Journal of Alloys and Compounds 1053 (2026) 186237

Contents lists available at ScienceDirect

Journal of Alloys and Compounds

journal homepage: www.elsevier.com/locate/jalcom

Low-cost austenitic complex concentrated alloy with deformation-induced plasticity and nanoprecipitate as a strategy to enhance energy absorption at cryogenic temperature: Computational modeling and experimental validation

Angelo Oñate [a,*], Juan Pablo Sanhueza [a], Diego Wackerling [a], Carlos Lanziotti [b], David Rojas [a], Víctor Tuninetti [c], Abdul Herrim Seidou [d]

[a] Department of Materials Engineering (DIMAT), Faculty of Engineering, Universidad de Concepción, Edmundo Larenas 315, Concepción, Chile
[b] Department of Mechanical Engineering (DIM), Faculty of Engineering, Universidad de Concepción, Edmundo Larenas 219, Concepción, Chile
[c] Department of Mechanical Engineering, Universidad de La Frontera, Temuco, Chile
[d] Metallic materials for Additive manufacturing, A&M Department, University of Liège, Liège 4000, Belgium

ARTICLE INFO

Keywords:
Phase prediction
Machine Learning
Complex concentrated alloys
Intermetallics
Twining

ABSTRACT

The development of multicomponent alloys for cryogenic applications requires reliable prediction of phase stability to ensure adequate toughness at low temperatures. This is critical to address the embrittlement phenomenon observed in conventional alloys under cryogenic conditions, as in the case of austenitic stainless steels such as 304 L and 316 L, which suffer toughness degradation due to the formation of martensitic (α') phase. In this context, the present work focused on the development of a complex concentrated alloy (CCA) based on the FeCrNiCuTiVC system, fabricated by induction melting under an argon-controlled atmosphere, using primarily recycled stainless steel and ferroalloys as raw materials. The alloy design was carried out through an integrated approach combining machine learning techniques (Random Forest and XGBoost) trained on a robust database of 2591 records, together with thermodynamic predictions via CALPHAD using the TCHEA6 database. The resulting alloy exhibited an austenitic matrix with fine-scale precipitate-like features and the formation of σ phase. Tensile tests revealed an elongation of ~82 % and a strength–ductility product (PSE) of 40.1 GPa·%, evidencing high damage tolerance. Nanoindentation and microhardness results indicated that the σ-phase precipitates do not exert a significant macroscopic effect in this alloy, which accounts for its remarkable deformability. Furthermore, nanoindentation tests revealed pop-in events characteristic of twinning, suggesting the activation of a twinning-induced plasticity (TWIP) mechanism. This was evidenced by SPM analyses of the nanoindentation imprint and by FE-SEM observations in the post-fracture sample. Similarly, fine-grained regions were identified in the area adjacent to the fracture, originating from subgrain formation caused by the severe dislocation interactions within the material. This explains the high ductility observed and validates the pronounced strain-hardening behavior of the alloy. Finally, Charpy impact tests demonstrated energy absorption of 205 J/cm^2 at room temperature and 226 J/cm^2 at 77 K, indicating not only excellent toughness at cryogenic temperatures but also the absence of a ductile-to-brittle transition, even in the presence of intermetallic phases. This behavior is attributed to the synergy between the TWIP mechanism and nanoprecipitates, both of which enhance the mechanical response and suppress premature embrittlement potentially induced by the σ phase, given its reduced fraction in the microstructure.

1. Introduction

Research on alloys with high energy absorption capacity, assessed through the strength elongation product and toughness testing, is of critical relevance for demanding applications in the automotive, aerospace, and energy sectors [1,2]. These parameters are key indicators of

* Corresponding author.
E-mail address: aonates@udec.cl (A. Oñate).

https://doi.org/10.1016/j.jallcom.2026.186237
Received 31 August 2025; Received in revised form 12 January 2026; Accepted 14 January 2026
Available online 14 January 2026

structural safety, and a deep understanding of the underlying physical phenomena governing the mechanical behavior of materials is essential for the design of advanced, application-specific functional alloys [3]. In this context, temperature plays a pivotal role in energy absorption under cryogenic operating conditions [3], where the material undergoes embrittlement due to the ductile-to-brittle transition. This phenomenon is primarily attributed to a substantial reduction in dislocation mobility, resulting from the lower thermal energy available to overcome internal energy barriers that hinder dislocation glide. Consequently, the critical stress required to activate dislocation slip increases, reducing the material's plasticity. These effects are particularly severe in systems with low atomic packing or limited slip systems. Accordingly, HCP and BCC crystal structures inherently exhibit ductile-to-brittle transition behavior [1]. However, this is not typically observed in FCC structures [1,4], owing to their high atomic packing density, availability of multiple slip systems, and greater control over grain size. These features reduce internal energy barriers for dislocation motion. Furthermore, although the critical stress for dislocation slips activation increases due to reduced thermal energy, FCC systems may accommodate alternative deformation mechanisms such as twinning [5], which significantly mitigates the ductile-to-brittle transition effect.

Twinning is further promoted by the temperature dependence of the stacking fault energy (SFE), which facilitates the formation and activation of twins and nanotwins in FCC alloys even at cryogenic temperatures as low as 77 K [1]. This characteristic enables FCC-structured alloys to be considered for applications involving the storage of liquefied fuels, such as liquefied petroleum gas (LPG) and hydrogen [4,6], which are currently stored in austenitic stainless steels such as 316 L or 304 L [7–13]. However, these conventional alloys possess rigid composition systems that limit the optimization of their mechanical performance under critical conditions such as cryogenic temperatures and hydrogen embrittlement. Moreover, the toughness of these materials deteriorates with decreasing temperature, a phenomenon commonly attributed to the $\gamma \rightarrow \alpha'$ martensitic transformation. Within this context, multicomponent systems such as high-entropy alloys (HEAs) and complex concentrated alloys (CCAs) offer the ability to overcome compositional constraints [4,5,14], enabling the development of materials with outstanding mechanical performance and thereby supporting the advancement of sustainable technological innovation [1,14,15].

Nevertheless, the development of multicomponent alloys remains a complex task, primarily due to their intricate compositional systems and the challenges associated with microstructural control [16–20]. For this reason, various phase prediction systems and methodologies based on machine learning have been implemented [20]. In recent years, phase prediction in multicomponent alloys using machine learning has significantly advanced by extending beyond conventional classifications such as solid solution, multiphase, intermetallic, and amorphous phases. These advancements now encompass multiclass predictions including structures such as FCC, BCC, HCP, FCC+BCC, FCC+IM, BCC+IM, FCC+BCC+IM, and IM phases [16,18–20]. To enable these developments, robust databases have been constructed and complemented by CALPHAD-based thermodynamic modeling for validation purposes [18,19].

Based on the previous discussion, the primary objective of this research is to design an austenitic complex concentrated alloy with precipitation strengthening, using supervised machine learning and parametric analysis, validated through CALPHAD thermodynamic modeling and experimental characterization. The alloy will undergo mechanical characterization at room temperature, and its ductile-to-brittle transition behavior will be evaluated through Charpy impact testing at cryogenic temperature using liquid nitrogen. Microstructural characterization will be conducted primarily through X-ray diffraction (XRD), scanning electron microscopy (SEM) coupled with energy-dispersive X-ray spectroscopy (EDS), and electron backscatter diffraction (EBSD).

2. Methodology

A complex concentrated alloy was designed using the parametric analytical model proposed in [19], ensuring the formation of an austenitic matrix through appropriate manipulation of the valence electron concentration (VEC). The Random Forest model, trained on a dataset of 2591 entries, was employed. The data were categorized as follows: FCC (496), BCC (617), BCC+FCC (197), FCC+IM (277), BCC+IM (205), FCC+BCC+IM (76), IM (368), HCP (72), BCC+HCP (85), and AM (198). A grid search optimization was performed to fine-tune the key hyperparameters of the Random Forest model, enhancing its predictive capacity. The number of trees in the forest was evaluated between 100 and 500. The optimal tree depth was configured with a minimum of 10 and increments of 20 levels, enabling the model to capture complex patterns. To address class imbalance, class weight adjustments were applied. Model validation was performed using 10-fold stratified cross-validation to ensure the representation of all classes within each fold. For the XGBoost model, hyperparameter optimization included tuning the learning rate within a range of 0.01–0.2 to control the speed of the learning process during training. The maximum tree depth was limited to 10 levels with 20-level increments, allowing the model to capture intricate data relationships. Similar to Random Forest, class weight adjustments were implemented to correct for class imbalance, and model validation was carried out using 10-fold stratified cross-validation to maintain class representativeness across all partitions. Finally, a soft voting classifier was implemented by combining the two best-performing models. Soft voting was employed, leveraging the probabilistic outputs of each base model rather than relying on discrete predictions. This ensemble approach improved the overall robustness and reliability of the decision-making process.

The high-entropy alloy was fabricated using ferroalloys of FeCr, FeC, FeTi, and FeV. Copper (Cu) and Nickel (Ni) were added as pure elements. The ingot was produced in an induction melting furnace under a controlled argon atmosphere. To achieve the controlled environment, a mechanical vacuum of 1×10^{-3} Torr was first established, followed by argon injection to reach an inert atmosphere with a constant flow rate of 5 L/min. Prior to melting, all raw materials were dried at 80 °C for 24 h to eliminate residual moisture. Chemical composition of the resulting alloy was determined using a Spectro–SpectroMAXx optical emission spectrometer. Four measurements were taken at different locations on the sample, and the significant values were averaged. The chemical composition results obtained from the cast sample are presented in Table 1.

The ingots were sectioned into 2 cm × 2.5 cm samples for subsequent heat treatments. The complex concentrated alloy was solution-treated at 1200 °C for two hours, followed by thermomechanical processing via hot rolling at 1200 °C until a 50 % thickness reduction was achieved. This was immediately followed by water quenching. A second solution treatment was then performed for two hours, also followed by water quenching. From this point onward, the sample is referred to as CCA1200.

For sample preparation, manual grinding was performed using silicon carbide sandpapers with mesh sizes ranging from 240 to 1200, followed by polishing with a 0.05 μm alumina suspension. The samples were chemically etched to reveal their microstructure. The chemical etching procedure consisted of using Vilella's reagent for a duration of 120 s.

Microstructural characterization was carried out using TESCAN VEGA 3 EASYPROBE SBU and JEOL JXA 8600 M scanning electron microscopes. SEM imaging was performed using both secondary

Table 1
Chemical composition (wt%) of design for the investigated high entropy alloys.

Alloy	Fe	Cr	Ni	Cu	Ti	V	C	Imp
CCA1200	35.89	27.10	27.58	4.76	1.44	2.27	0.10	Bal.

electron (SE) and backscattered electron modes (BSE) at an acceleration voltage of 20 kV and a working distance of approximately 10 mm. Elemental analysis was conducted via energy-dispersive X-ray spectroscopy to identify the chemical phases and precipitates present. Additionally, X-ray diffraction (XRD) was employed for phase identification using Cu radiation and a Ni Kβ radiation filter, with an acceleration voltage of 40 kV and a working current of 20 mA. The measurement range was set between 30° and 90°, with a step size of 0.02° and a scanning speed of 1.2°/min. The lattice parameter was determined using Eq. (1)

$$a = \frac{\lambda\sqrt{h^2 + k^2 + l^2}}{2\sin\theta_{hkl}} \tag{1}$$

The stacking fault energy of the compositional system was calculated using Eq. (2):

$$SFE = \frac{K_{111}\omega_0 G_{111}\alpha_0 A^{-0.37}}{\pi\sqrt{3}}\frac{\varepsilon^2}{\alpha} \tag{2}$$

Where $K_{111}\omega_0$ is the proportionality constant, equal to 6.6, α_0 is the lattice parameter obtained via X-ray diffraction; A is the Zener anisotropy factor $\left(A = \frac{2C_{44}}{C_{11}-C_{12}}\right)$; and G_{111} is the shear modulus in the (111) plane $\left(G_{111} = \frac{C_{44}+C_{11}-C_{12}}{3}\right)$. ε denotes the microstrain, determined through Williamson-Hall analysis based on the XRD peak profiles using Origin Lab Software; α represents the stacking fault frequency, which is measured by analyzing a stress-free sample and a sample subjected to 5% strain, using Eq. (3) [21–23].

$$(2\theta_{200} - 2\theta_{111})_{5\%} - (2\theta_{200} - 2\theta_{111})_{0\%} = \frac{-45\sqrt{3}}{\pi^2}\left(\tan\theta_{200} + \frac{1}{2}\theta_{111}\right)_{0\%}\alpha \tag{3}$$

Microhardness tests were performed using a Leco instrument with a 300-gram load and a Vickers indenter. Five indentations were carried out, and the reported values correspond to the average of these measurements.

Similarly, the stacking fault energy was calculated using the method proposed by Olson and Cohen [24] according to Eq. 7:

$$SFE = 2\rho\Delta G^{\gamma\to\varepsilon} + 2\sigma \tag{7}$$

where ρ is the molar density, $\Delta G^{\gamma\to\varepsilon}$ is the Gibbs free energy difference between austenite and hexagonal close-packed martensite, and σ is the interfacial energy. In this study, an interfacial energy of 12 mJ/m^2 was used, assuming a coherent interface [24].

Tensile tests were performed in triplicate according to the ASTM E8 standard. Mechanical characterization was carried out at a strain rate of 1 mm/min using an INSTRON 8801 universal testing machine. Flat specimens with a calibrated gauge section of 2 × 3 mm were employed. The results were reported in true stress–strain components using the following equations:

$$\sigma_v = \sigma_{ing}(1 + \varepsilon_{ing}) \tag{8}$$

$$\varepsilon_v = \pm\ln(1 + \varepsilon_{ing}) \tag{9}$$

Where σ_v is the true stress, σ_{ing} is the engineering stress, ε_v is the true strain, and ε_{ing} is the engineering strain.

To analyze the nanoscale mechanical response, nanoindentation was performed using a Hysitron TI 980 nanomechanical tester. Nanoindentation tests were conducted at room temperature through single-point indentation and quantitative high-speed mechanical property mapping (XPM). The single-point test conditions consisted of 60 s loading cycles, including 15 s loading, 30 s of hold time at peak load, and 15 s of unloading. XPM characterization was carried out using the same loading cycle parameters, with a 2 μm spacing between indentations and a scanning speed of 10 μm/s. A Berkovich indenter tip with $\nu_i = 0{,}07$ and $E_i = 1140$ GPa was used for all measurements. Tip calibration was performed on a fused quartz standard, and nanoindentation data were analyzed following the Oliver and Pharr method [25,26] as described in Eq. (10).

$$A_c(h_c) = C_1 {h_c}^2 \tag{10}$$

Where h_c is the contact depth and A_c is the projected contact area of the indentation, with the constant C_1 equal to 25.4. Likewise, the contact depth can also be obtained from the unloading stiffness using Eq. (11).

$$h_c = h_{max} - \varepsilon\frac{P_{max}}{S} \tag{11}$$

Where h_{max} corresponds to the maximum displacement of the indenter, ε is a constant that depends on the indenter geometry and equals 0.75 for a Berkovich indenter [26–30], P_{max} is the maximum applied load, and S is the contact stiffness determined from the slope of the P-h curve during the initial portion of the unloading segment.

To evaluate the energy absorption capacity of the CCA1200 alloy, Charpy impact tests were conducted using a Mohr & Federhaff AG Mannheim pendulum impact machine equipped with a dial gauge for energy absorption readings. The specimens were prepared in accordance with ASTM E23. Each specimen measured 55 mm in length, with a width and thickness of 10 mm. A V-notch was machined at the center of each specimen, with a depth of 2 mm, a root radius of 0.25 mm, and an opening angle of 45°. Tests were performed at both room temperature and cryogenic temperature. Cryogenic testing was carried out by immersing the specimens in liquid nitrogen at 77 K for 15 min, followed by immediate testing within a maximum of 6 s after removal from the liquid nitrogen. All tests were performed in triplicate.

3. Analysis and results

The results of the parametric calculations performed for the CCA1200 alloy are presented in Table 2. Analysis of these results shows that, according to Poletti et al. [31], since the alloy exhibits a VEC greater than 7.5 and an e/a ratio below 1.8, the stable phase should be FCC. Likewise, as proposed by Dong et al. [32], if dx < 0.117, the formation of TCP phases would not be expected. Based on this, for the CCA1200 alloy, with a dx of 0.12, intermetallic compounds are predicted to form. This observation is further supported by the criterion proposed by Wang et al. [33,34], and validated by Oñate et al. [17], which indicates that the formation of intermetallics occurs when $\gamma > 1.175$.

Moreover, Tsai et al. [35], reported that multicomponent alloys are prone to sigma phase formation when PSFE exceeds 42.5 and the VEC lies between 6.88 and 7.84. Based on these criteria, the CCA1200 alloy falls outside the VEC evaluation range and therefore should not form sigma phase under these mutually exclusive conditions. The present authors consider the combined use of VEC and PSFE to be highly valuable, given its rigorous formulation and application. However, exceptions may arise, primarily associated with VEC, as this parameter strongly depends on the specific compositional system. Consequently, VEC should be considered as an isolated descriptor for sigma phase prediction, whereas PSFE remains a reliable indicator of its likelihood.

In this context, it is noteworthy that the CCA1200 alloy investigated in this study, with a PSFE of 62.61, exhibits a high probability of sigma phase formation as an intermetallic compound. Finally, given that the atomic size mismatch calculated for this alloy is below 5.23, and according to the findings of Oñate et al. [19], the formation of an ordered B2 phase such as FeTi or NiTi should not be expected.

The results of multicategorical phase prediction using machine learning, following the method reported in [19], indicated that the stable phase in the alloy is FCC with an accuracy of 55 % (see Fig. 1), consistent with the outcome of the parametric analysis proposed by

Table 2
Results of parametric calculations for CCA1200.

VEC	e/a	Dr (%)	dx	dHm (kJmol-1)	dSm (Jmol-1K-1)	Gamma	Ohm	PSFE (%)
7.91	1.66	3.58	0.12	-4.26	11.59	1.89	5.17	62.61

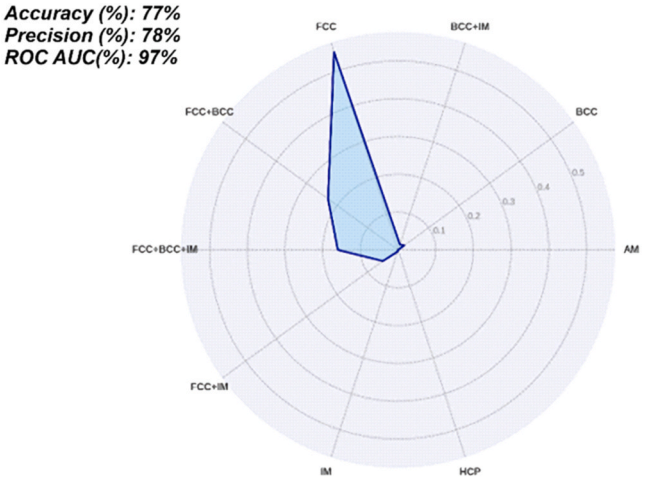

Fig. 1. Results obtained from phase prediction using an ensemble machine learning model.

Poletti et al. [31]. Nevertheless, as highlighted by Oñate et al. [18,19,36], phase predictions obtained through machine learning must be cross-validated with the packing factor γ. Specifically, if the packing factor exceeds 1.175, as originally proposed by Wang et al. [34], the alloy will possess sufficient driving force for the formation of intermetallic phases. Therefore, the combined results from machine learning and the γ packing factor suggest that the stable phase in the CCA1200 alloy is FCC + IM.

The results previously obtained and validated through CALPHAD computational simulations are shown in Fig. 2. The phase diagram reveals an alloy with a predominantly austenitic matrix, thereby confirming the outcomes derived from the parametric analysis proposed by Poletti et al. [31]. In addition, the presence of thermodynamically stable intermetallics of the $L1_2$ (γ'), B2, and σ types is observed across different temperature conditions under thermodynamic equilibrium. It should be emphasized that $L1_2$ or B2

type nanoprecipitates are more likely to be observed, as they exhibit rapid nucleation kinetics and a relatively low growth rate. In contrast, the σ phase is characterized by sluggish nucleation, but once formed, it undergoes pronounced growth and dominant coarsening behavior. These results are consistent not only with the parametric predictions but also with the machine learning predictions coupled with the γ packing factor.

It is important to note that the $L1_2$ phase exhibits high stability at elevated temperatures, diminishing as the σ and γ'_2 (η) phases become stabilized. The γ' phase in the CCA1200 alloy is expected, as it was designed based on thermodynamic affinity under metallurgical considerations involving Ni, Cu, and Ti. Han et al. [37] for example, reported Ni- and Ti-rich γ' precipitates, where Co promoted the homogeneous dispersion of γ' within the FCC matrix. The γ' phase possesses a primitive

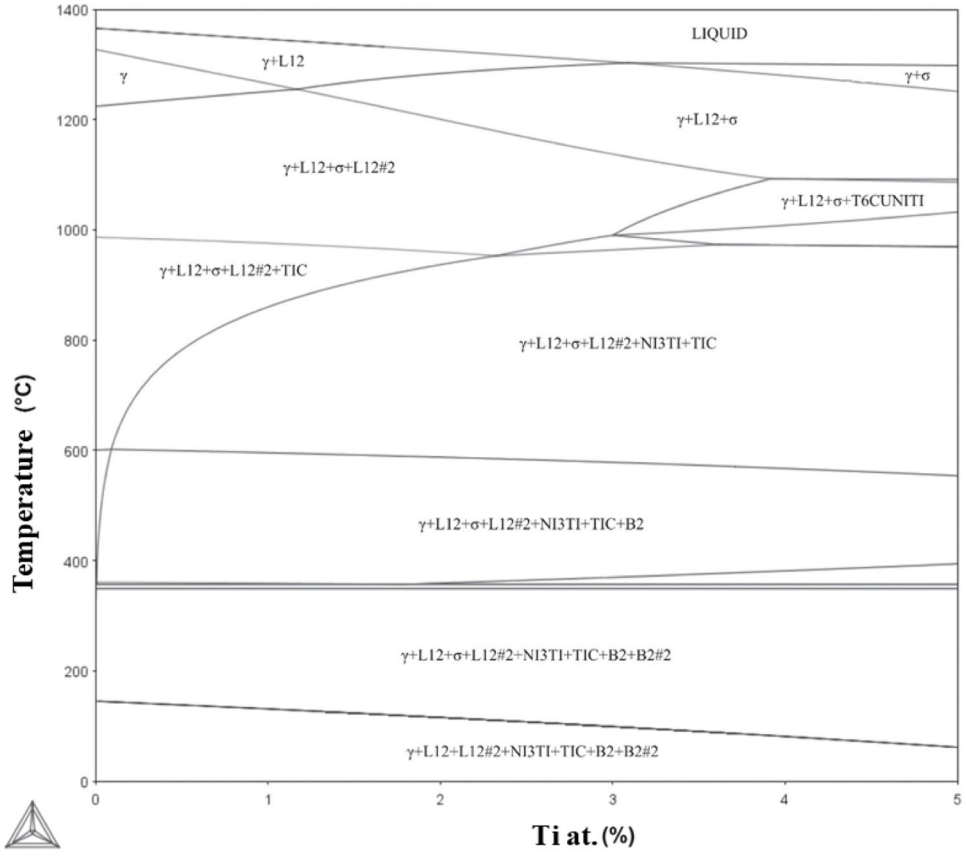

Fig. 2. Phase diagram of the CCA1200 alloy.

cubic structure with an A_3B stoichiometry, where A corresponds to Ni or Cu, and B is typically Ti or Al [38,39] The η (Ni_3Ti) phase derives from γ′ and is characterized by a hexagonal crystal structure [40] sharing the same stoichiometry as γ′ but occurring in a stable, acicular morphology [41]. The B2 phase, in contrast, follows an AB stoichiometry, with elements drawn from Groups IV through XIII [42–44]. Finally, the σ phase exhibits an AB structure where A corresponds to elements from Groups VA and VIA (V, Cr, Mo, Ta, W, Nb), while B consists of Fe, Mn, Co, and Ni [45].

The sigma phase is highly thermodynamically stable with a PSFE of 62.61, which can be attributed to the high Cr and V content in the alloy. The $L1_2$ and B2 phases are also thermodynamically stable, although they are energetically competitive with each other. The $L1_2$ phase may form as Ni_3Ti, while the B2 phase may form as NiTi or FeTi. Although Thermo-Calc predicts B2 as a stable phase, Oñate et al. [19] proposed that B2 stability should only be expected when the atomic size mismatch is equal to or greater than 5.23, which is not the case for this alloy. While a record in [19] reported B2 formation at an atomic size mismatch of 4.2 %, such a condition is considered unlikely in multicomponent alloys. Based on this, the Ni_3Ti phase should be energetically more favorable than the B2 phase, which may only achieve stability if the system's kinetic conditions allow it.

Fig. 3 and Table 3 show the X-ray diffraction results for the CCA1200 sample. The data indicate the presence of a γ phase accounting for 98.51 wt% and a σ phase accounting for 1.49 wt%, with no detectable B2 phase. The refined phase parameters obtained through Rietveld analysis are listed in Table 3.

Fig. 4 presents the results obtained by atomic force microscopy, revealing the presence of nanoprecipitates with a highly homogeneous distribution dispersed throughout the matrix (see Fig. 4.b). These precipitates exhibit sizes ranging from 40 to 350 nm, with the highest concentration between 50 and 100 nm (see Fig. 4.c). It is noteworthy that, due to their pseudo-spherical geometry and homogeneous dispersion within the matrix, these precipitates could provide effective strengthening through dislocation entanglement during plastic deformation.

The SEM results for the CCA1200 alloy are presented in Fig. 5. The observed precipitates correspond primarily to the σ phase and, to a lesser extent, titanium carbide precipitates. The σ phase was characterized by a chromium-to-iron ratio ranging from 1.03 to 1.24. Therefore, considering the distortion introduced by the excitation volume on the EDS results, it is regarded as consistent with the σ-phase AB(Cr,Fe) polytype. The detailed chemical composition of each analyzed region is

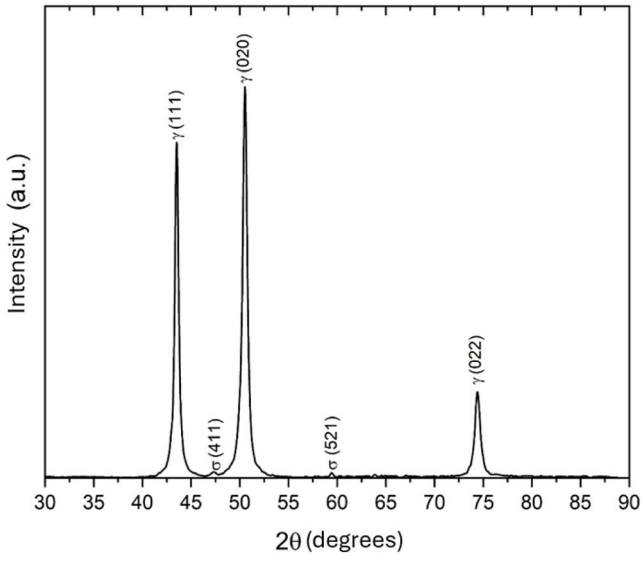

Fig. 3. X-ray diffraction results for the CCA1200 alloy.

Table 3
X-ray diffraction results for the CCA1200 alloy.

Phase	2Θ (°)	Space group	Lattice parameter [Å]	Calculated lattice parameter [Å]	wt%
γ(111)	43.7	Fm-3m	3.58	3.58	98.51
γ(020)	50.5	Fm-3m	3.58	3.61	
γ(022)	74.5	Fm-3m	3.58	3.59	
σ(CrFe) (411)	47.3	P42-mnm	8.19	8.14	1.49
σ(CrFe) (521)	59.6	P42-mnm	8.19	8.48	

provided in Table 4. Moreover, the morphology of the phase is consistent with that reported by other authors in multicomponent austenitic systems [46,47].

The hardness results obtained for the CCA1200 alloy are summarized in Table 5. These values are consistent with the reported hardness range for FCC alloys doped with C [48] and the low deviation among the measurements indicates a minor influence of the secondary phases that did not fully dissolve.

The nanoscale response of the CCA1200 alloy is shown in Fig. 6. The nanoindentation response of the CCA–1200 alloy (see Fig. 6b) exhibits slight pop-in events, characteristic of localized constraints on plastic flow. The nonlinearities observed are indicative of submicrometric-scale twinning processes when located in the high-load regions of the P–h curve [49]. It is important to note that pop-ins may also occur due to phenomena such as dislocation activation, the nucleation of new dislocations, and pile-up processes within the alloys [50,51]. Nevertheless, these events generally appear in the early regions of the P–h curve, specifically those occurring below 250 μN. In this context, the initial pop-ins are associated with dislocation activation and glide (below 250 μN), whereas subsequent events may be related to pile-up phenomena or twinning, as observed in Fig. 6a through SPM analysis, and as reported in the literature [52,53]. In this case, the pop-ins in the upper regions of the P-h curve in Fig. 6b are attributed to mechanical twinning, based on the evidence presented in Fig. 6a, or a mixed mechanism involving both twinning and pile-up.

Based on the foregoing discussion, the stacking fault energy (SFE) calculated for the CCA1200 compositional system using JMatPro was 32.25 mJ/m^2. In contrast, thermodynamic analysis following the Olson and Cohen approach with Thermo-Calc (SSOL8 database) yielded an SFE of 49.95 mJ/m^2. Both calculated values fall within the expected range for twinning activation, thereby supporting the observations shown in Fig. 6.a and 6.b.

Although traditional activation thresholds for deformation twinning are typically reported between 20–45 mJ/m^2, studies have shown that for SFEs ranging from 45 to 60 mJ/m^2, twinning remains operative through the formation of deformation microbands (TWIP/MBIP) [54]. Nevertheless, using Eq. (2) and X-ray diffraction treatment, the experimentally determined SFE for the CCA1200 alloy was 22.5 mJ/m^2, based on the parameters listed in Table 6. On this basis, twinning is expected to occur in the alloy. However, it is likely that under the applied nanoindentation load conditions, only nanoscopic twinning is induced within the FCC structure. This could explain the low-intensity pop-in response.

The nanohardness value obtained for the alloy was 4.96 ± 0.9 GPa. These results are consistent with those reported by Fan et al. [55] who measured an average nanohardness of 4.51 GPa for the FCC structure, and by Shen et al. [56] who reported a nanohardness of 5.76 GPa for the same structural type.

The difference in the SFE values obtained through simulations using JMatPro and Thermo-Calc arises from the internal calculation frameworks of each program. JMatPro relies on semi-empirical models and proprietary databases primarily developed for conventional alloy systems; therefore, its accuracy may decrease when a large number of principal alloying elements are present, as is the case for multicomponent alloys. Nevertheless, it provides a useful initial reference during the

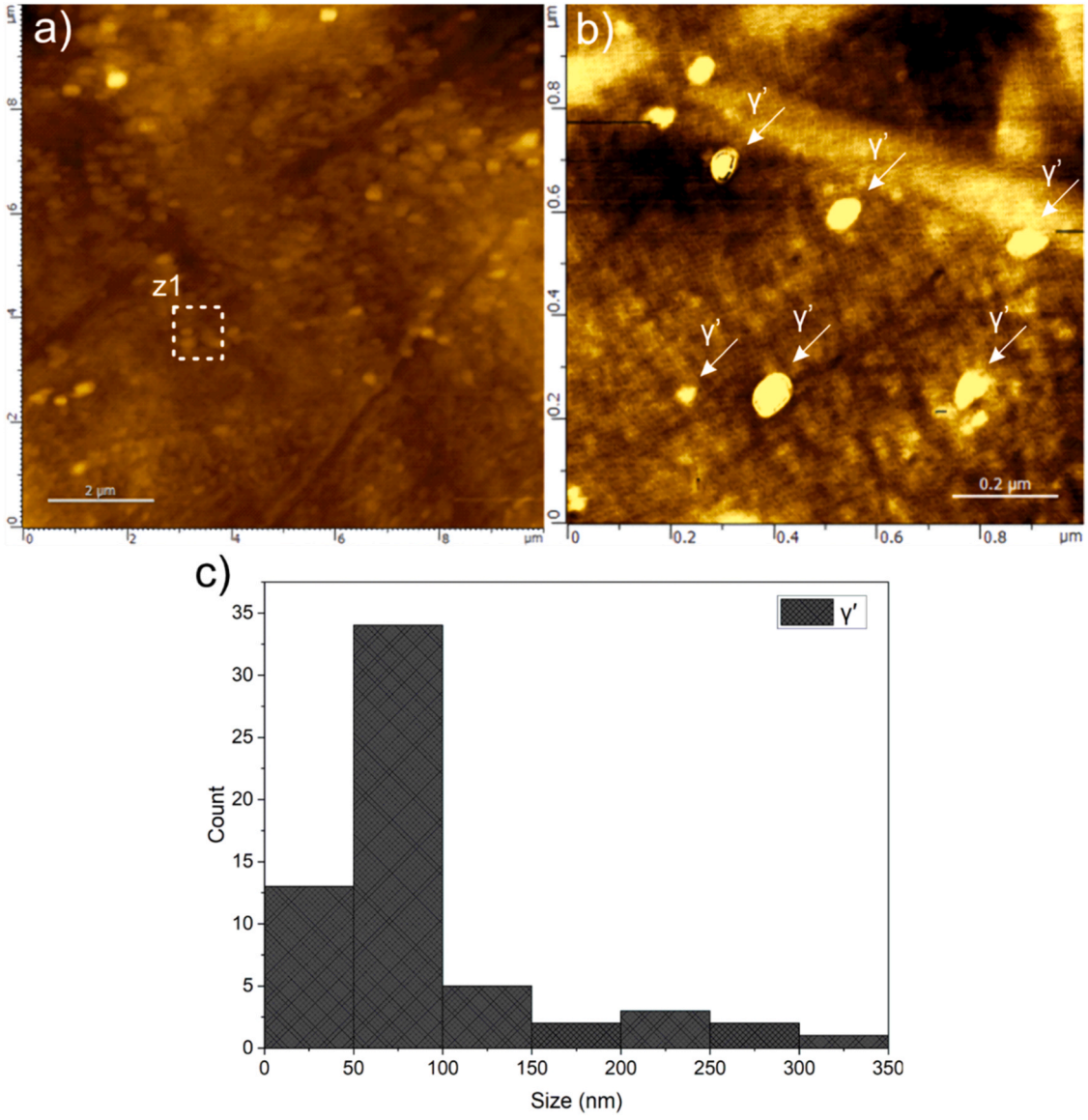

Fig. 4. Atomic force microscopy images of the CCA1200 alloy: a) SPM image showing the general microstructure; b) SPM detailed visualization of the nano-precipitates in the Z1 region; c) histogram of the nanoprecipitate size distribution.

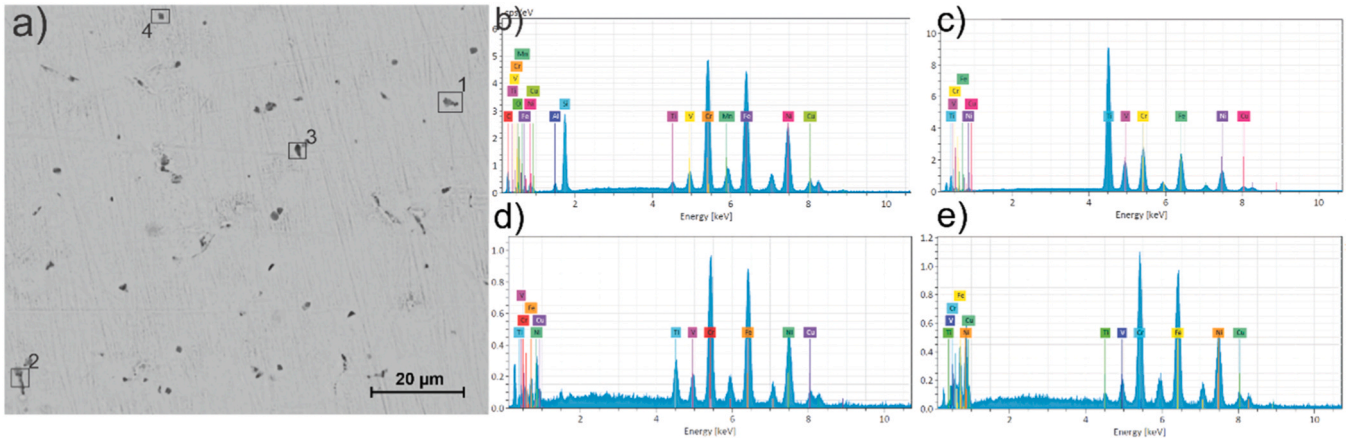

Fig. 5. Phase identification by scanning electron microscopy and energy-dispersive spectroscopy in the CCA–1200 alloy: (a) CCA–1200 at 2000 × magnification; (b) EDS spectrum of zone 1; (c) EDS spectrum of zone 3; (d) EDS spectrum of zone 2; (e) EDS spectrum of zone 4.

Table 4
Summary of EDS results obtained from Fig. 5.

Zone	Phase	Fe	Cr	Ni	Cu	Ti	V
1	σ(Cr,Fe)	29.60	28.62	28.3	5.54	4.92	3.02
2	σ(Cr,Fe)	34.69	27.93	27.73	5.61	1.10	2.94
3	σ(Cr,Fe)	35.59	28.89	27.26	4.91	0.66	2.69
4	MX(Ti,C)	22.80	16.93	16.73	3.10	37.47	2.97

Table 5
Summary of hardness and microhardness results for the CCA1200 alloy.

Alloy	Hardness (HRB)	Microhardness (HV)
CCA1200	66.9 ± 3	124 ± 5

early stages of alloy design. In contrast, Thermo-Calc determines SFE based on Gibbs free energy calculations and explicitly considers interface characteristics, making it a highly sensitive computational approach capable of capturing subtle deviations. This has been supported by Aguilar et al. [57]. Furthermore, experimental SFE values are strongly associated with the chemical composition of the material and the level of deformation or lattice distortion, as reported by Woo et al. [58].

The nanoindentation results are presented in Fig. 7. Fig. 7.a shows the stress–strain curve obtained from the test, reaching a maximum stress of approximately ~17 GPa. As the indenter continues to penetrate the sample, the stress progressively decreases without exhibiting premature stabilization a typical phenomenon in materials with low or negligible strain-hardening capacity, as documented in [59]. This behavior indicates a high strain-hardening capability in the alloy, attributed to the presence and distribution of nanoprecipitates within the matrix. Fig. 7.b displays the characteristic creep strain–time curve obtained during the nanoindentation creep test.

Fig. 7.c presents the creep strain-rate curve as a function of time. It can be observed that the transient time is approximately ~1.5 s, after which the response becomes stable. The behavior within the transient regime is dynamic and complex due to mechanisms associated with dislocation interactions and nanomacro-twinning under multiaxial conditions beneath the indenter [60]. Based on this, the transient behavior highlighted in Fig. 7.c with upward-pointing black arrows in the magnified region can be attributed to the combined effects of nanoprecipitates and nanotwinning interacting with dislocations through a dynamic recovery mechanism.

Fig. 7.d shows the strain-rate sensitivity of the alloy, characterized by a value of m = 0.0255. This value falls within the typical range reported for FCC high-entropy alloys. In austenitic systems, higher strain-rate sensitivity values are expected because plastic deformation is less localized, in contrast to BCC structures where plastic deformation tends to localize more severely. Feng et al. [61], reported an m value of 0.035 for an FCC CoCrFeNiCu high-entropy alloy, which is 27.14 % higher than the value obtained in the present study, indicating a lower degree of shear-stress localization [62,63].

Regarding the strain-hardening coefficient (n), a value of n = 39.21 was obtained for the CCA1–1200 alloy, which is higher than values reported at room temperature under similar loading conditions. For example, Sharma et al. [64], reported n values of 31 for CNA and 33 for SNA in ferritic–martensitic systems. In the same context, Sadeghilarindjani et al. [65], obtained an n value of ~28 for a CoCrFeMnNi alloy at room temperature. In metallic alloys, an increase in the strain-hardening coefficient is primarily associated with greater difficulty in dislocation glide (particularly when $n > 3$), which serves as an indicator of enhanced local restriction to dislocation motion and a larger contribution of dislocations activated by stresses beneath the indenter, as well as the continuous generation and annihilation of dislocations [66]. In this regard, Han et al. [60], reported an *n* value of 27.9 at room temperature under a load of 2000 μN in a γ/γ' high-entropy alloy with the compositional system $Al_{10,2}Co_{16,9}Cr_{7,4}Fe_{8,9}Ni_{48,3}Ti_{5,8}Mo_{0,9}Nb_{1,2}W_{0,4}$. It should be noted that the *n* values reported in that study correspond to loads between 1000 and 3000 μN, whereas the present work employed a maximum load of 500 μN. It is well established that increasing the applied load during nanoindentation generally leads to higher *n* values, as the enhanced dislocation activity and strengthening mechanisms promote a higher creep rate. Within this context, the *n* value obtained in this study exceeds those of many conventional compositional systems and high-entropy alloys strengthened by nanoprecipitates. This suggests a strong contribution from secondary hardening mechanisms, such as the formation of nanotwins—an aspect that should be thoroughly evaluated in future work through detailed transmission electron microscopy analyses.

As previously discussed, the phenomena of lower strain-rate sensitivity and higher strain-hardening coefficients are primarily associated

Table 6
Parameters obtained for the experimental calculation of stacking fault energy.

C_{11}	C_{12}	C_{44}	α	A	G_{111}	ε^2_{111}
226.64	133.77	119.34	$5.6x10^{-3}$	2.57	70.73	$4.79x10^{-6}$

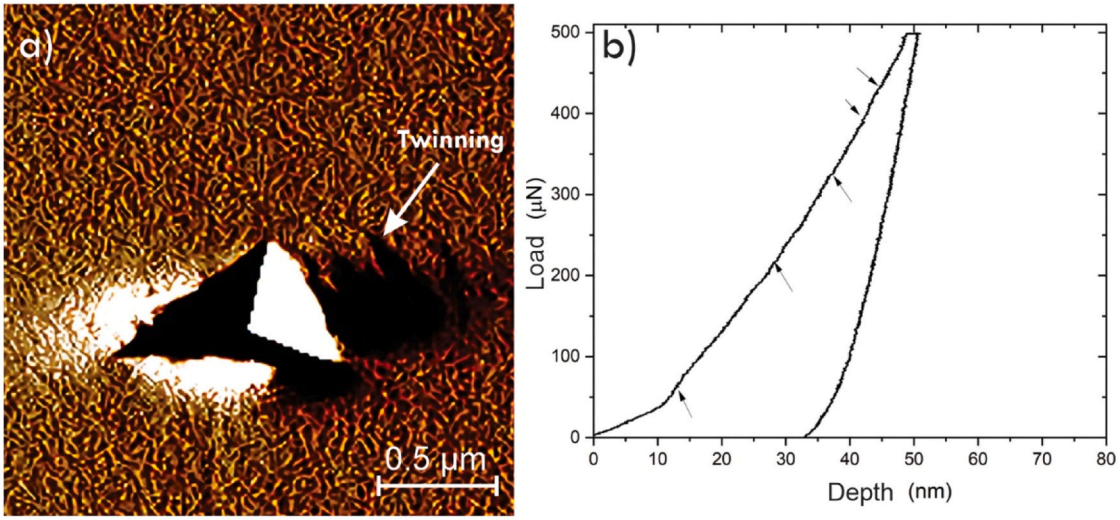

Fig. 6. Nanoindentation results for CCA1200: a) SPM image of the indentation imprint; b) load–displacement (P–h) curve.

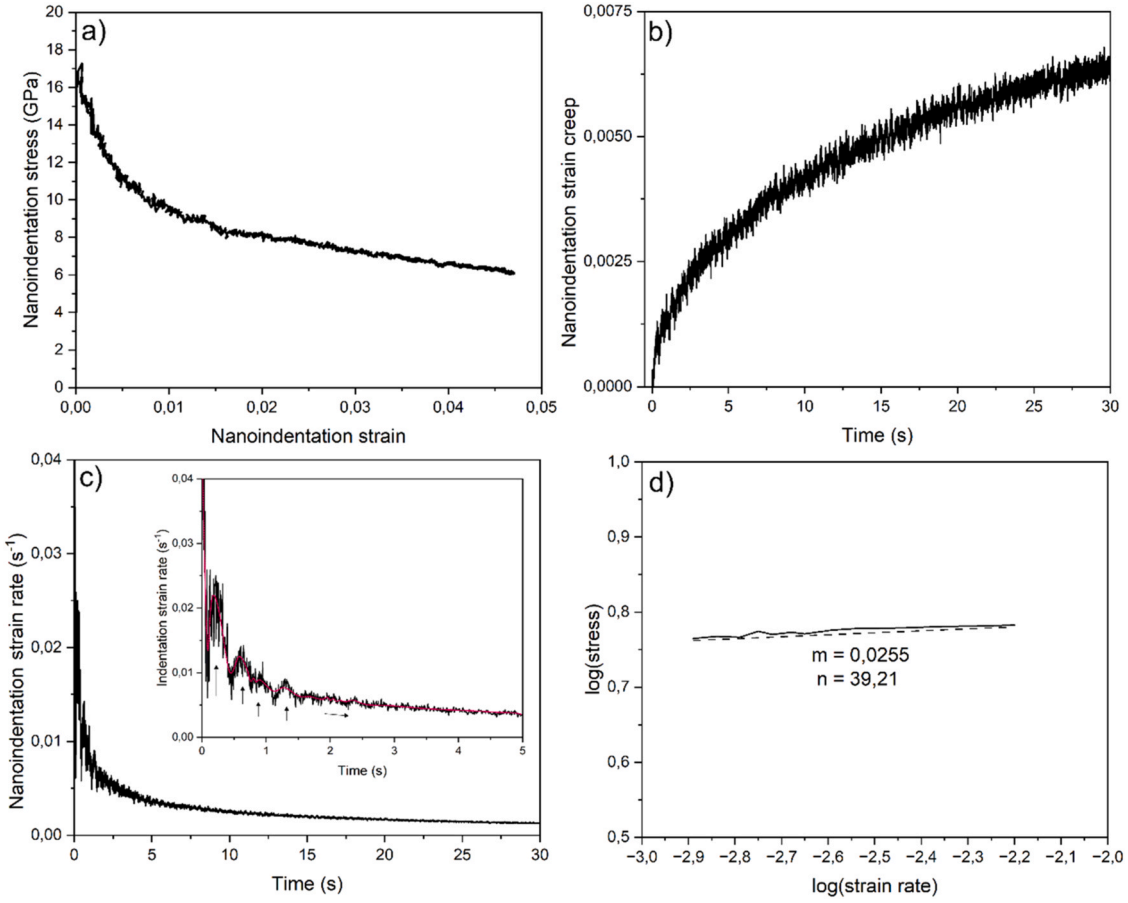

Fig. 7. Nanoindentation creep results for the CCA1200 alloy: a) stress–strain curve; b) creep strain vs. time curve; c) strain-rate vs. time curve; d) log–log plot.

with the interaction between dislocations and nanoprecipitates, which predominantly range from 50 to 100 nm in size. These nanoprecipitates provide an effective strengthening mechanism that explains the observed effects on the m and n values, consistent with the findings reported by Mozafari et al. [49], thereby validating the role of nanoprecipitates in the CCA1200 alloy. Similarly, dislocation glide and propagation under severe plastic-strain localization generate a stress state conducive to the formation of nanotwins, as observed in Fig. 6, a

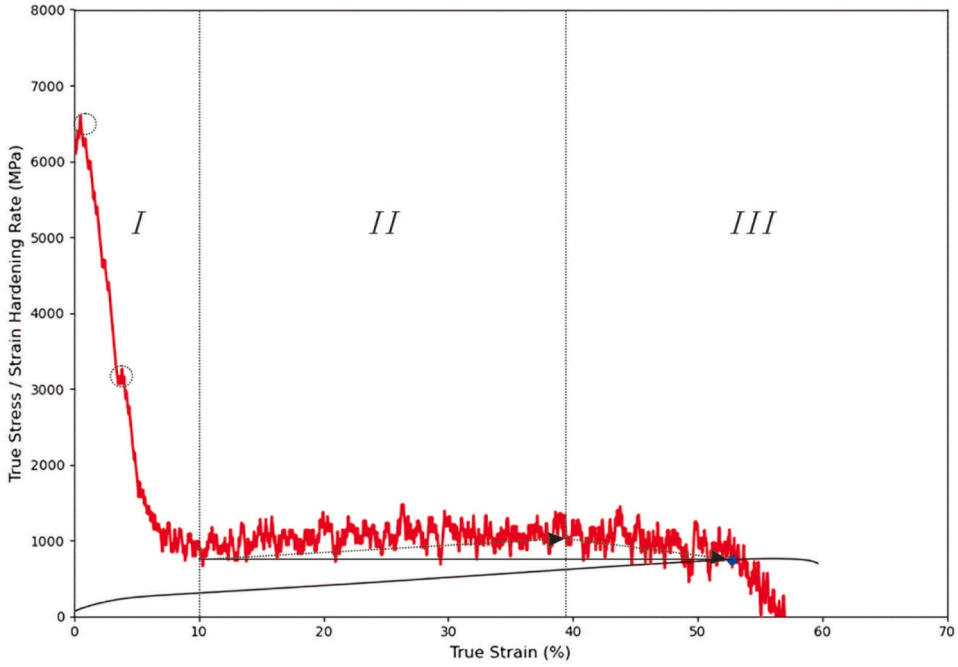

Fig. 8. Tensile mechanical response of the CCA1200 alloy.

process enabled by appropriate control of the stacking-fault energy (SFE) [67] and the degree of plastic-strain localization [68]. This behavior is supported and validated by the work of Fan et al. [68], in a high-entropy alloy with the compositional system $Fe_{18,36}Mn_{19,57}Co_{20,02}Cr_{21,10}Ni_{19,54}C_{0,6}N_{0,81}$ and by Zeng et al. [69] in a FeCrCoNi high-entropy alloy. Likewise, the high strain localization produced under severe plastic deformation can promote the nucleation of nano-grains within the micropore coalescence region at the fracture crest, a phenomenon corroborated by Pan et al. [70], in a Ti6Al4V alloy.

Based on the tensile results obtained (See Fig. 8), a PSE of 40.10 GPa % was calculated, indicating a high damage-tolerance index. This level of damage tolerance is suitable for aerospace applications, as it falls within the required range and exceeds the PSE values of alloys commonly used in aerospace and energy systems. He et al. [71] reported a PSE of 42.66 GPa% in a (FeCoNiCr)94Ti2Al4 FCC+ γ' alloy, with an ultimate tensile strength (UTS) of 1094 MPa and a strain of 39 % after cold rolling, annealing, aging, and quenching. The mechanical response achieved in this study for the CCA1200 alloy (see Table 7) is comparable to that reported in [71] for the FeCoNiCr and (FeCoNiCr)94Ti2Al4 systems in the solution-treated condition, which exhibited UTS values of 450 and 500 MPa, with fracture ductilities of 67 % and 69 %, respectively. However, while the UTS of the CCA1200 alloy was 492.21 MPa at the upper end of the aforementioned range, the fracture ductility reached 81.46 %, which is 18.06 % higher. These results position the CCA1200 alloy among the most ductile multicomponent austenitic alloys reported in the mechanical property survey by Li et al. [72]. Furthermore, Park et al. [73], investigated the mechanical performance of alloys commonly employed in liquefied natural gas (LNG) and hydrogen storage tanks. The alloys examined included AA5083, 304 L stainless steel, and Invar, with corresponding PSE values of 3.90 GPa%, 41.08 GPa%, and 20.40 GPa%, respectively. The PSE of the CCA1200 alloy was only 2.4 % lower than that of 304 L stainless steel, a difference that is not significant. Moreover, the PSE of CCA1200 could potentially be enhanced through thermal treatments that promote precipitation mechanisms, thereby improving strain-hardening behavior without compromising secondary strengthening mechanisms such as twinning. This approach could enable the CCA1200 alloy to surpass the PSE of conventional austenitic alloys like 304 L, which are currently employed in cryogenic storage systems.

The strain-hardening curve shows, in the initial stage, a hardening rate of 6200 MPa with an instantaneous increase to 6500 MPa at the early stage. This behavior is attributed to premature strain-hardening mechanisms arising from the interaction between dislocations and nanoprecipitates, a phenomenon that reappears during Stage I at ~4.2 % strain. Subsequently, a sharp drop in strain hardening is observed, associated with the dislocation slip mechanism, which dominates while secondary slip systems are activated and dislocation density increases, a process that stabilizes at ~10 % strain. Thereafter, Stage II occurs, characterized by a renewed increase in strain hardening up to 39 % strain, indicating the activation of additional strengthening mechanisms such as twinning or phase transformation [74]. Beyond 39 % strain (Stage III), a slight decrease in strain hardening is observed up to ~53 % strain, at which point necking occurs in the material. This behavior suggests that the alloy loses its ability to harden faster than it deforms, primarily due to mechanisms such as dislocation annihilation and rearrangement. Finally, once the sample surpasses 53 % strain, the strain-hardening capacity is completely exhausted. The Considère criterion is satisfied at a true strain of 53 % and a true stress of 748 MPa, represented by a blue marker in Fig. 8.

Table 7
Mechanical properties of the CCA1200 alloy under different heat treatment conditions.

Temperature °C	YS MPa	UTS MPa	ME%	PSE GPa%
CCA1200	225.12	492.21	81.46	40.10

The uniaxial tensile results for the CCA1200 alloy under different heat treatment conditions are summarized in Table 7.

Fig. 9 shows the tensile fracture zone of the CCA1200 alloy. Prominent slip bands can be observed, many of which exhibit severe surface striations resulting from the extensive plastic deformation. The presence of such slip bands is indicative of uniform deformation, which is consistent with the high ductility observed in the tensile tests. Furthermore, the slip band angles in the fracture regions were measured at 43 $\pm$ 4°, characteristic of dislocation slip under uniaxial tensile loading and corresponding to the maximum shear angle. Additionally, a secondary slip band orientation was identified at 25 $\pm$ 4°. These results are consistent with those reported by Li et al. [75] who provided further insights into fracture mechanisms in high-entropy alloys.

These results indicate the presence of two preferential stress orientations in the CCA1200 alloy, reflecting a homogeneous deformation capacity throughout the entire plastic regime. The high intensity observed in the primary slip bands accounts for the principal stress along that direction, which is consistent with the preferential orientation of microcracks and the maximum shear stress angle resulting from preferential dislocation slip in this type of structure. These primary slip bands also exhibit a discontinuous damage pattern, which is associated with a high energy absorption rate, thereby mitigating the onset and severe propagation of cracks. In contrast, the secondary slip bands are associated with discontinuities formed by damage propagation or plasticity lines interacting with precipitates, leading to a change in slip angle.

In Fig. 10, various deformation-induced effects can be observed in the region adjacent to the fracture surface of the CCA1200 alloy. Fig. 10.a shows twinning within the austenitic matrix, generated by the high deformation levels and the controlled stacking-fault energy (SFE) of the alloy, thereby validating the SFE ranges predicted through CALPHAD modeling and confirmed experimentally. In Fig. 10.b, a region near the fracture is shown containing intermetallics previously identified as σ-phase, along with nanoprecipitates in the matrix, which are more clearly visible in the magnified view of zone Z2. These observations are consistent with the results obtained earlier via atomic force microscopy. Fig. 10.c displays σ-phase in the vicinity of the fracture, exhibiting clear evidence of damage but without the presence of microcrack or crack propagation within the matrix. This behavior reflects the high energy-absorption capacity of the alloy and explains its ability to sustain very high deformation levels (81.46 %) despite containing intrinsically brittle intermetallic phases such as σ. Finally, Fig. 10.d shows zone Z2 corresponding to a twin structure magnified at 52,600 ×, revealing the formation of nanotwins. This finding is consistent with the behavior reported by Wang et al. [76] in Cu. Sun et al. [77], conducted a comprehensive review of nanotwin formation in FCC systems, indicating that alloys subjected to severe plastic deformation accompanied by twinning are highly likely to exhibit nanotwinning. Nanotwins have also been reported in high-manganese steels, such as Fe20Mn3Al3Si [78]. Moreover, Huang et al. [79], observed nanotwinning in a high-entropy alloy with a CoCrFeNi compositional system fabricated via laser powder bed fusion, where nanotwins formed under varying strain rates during tensile-fatigue testing.

Fig. 11 shows the microstructural features in the region adjacent to the fracture, where a highly plastically deformed texture is observed. In Fig. 11.a, small areas resembling fine grains can be seen along the surface bordering the fracture zone. Two regions were selected for higher-magnification analysis, designated as Z1 and Z2. In Fig. 11.b, corresponding to Zone Z1, grains with sizes between 1 and 2 μm are visible, indicating a grain-refinement effect induced by severe plastic deformation in the CCA1–1200 alloy. Li et al. [80], reported a similar phenomenon in a Ni-based superalloy fabricated by laser powder bed fusion (LPBF) and subjected to high-cycle mechanical fatigue, where fine-grain areas (FGA) were observed locally in near-surface regions adjacent to the crack. They attributed this refinement to cyclic loading and noted that FGAs do not typically form under fatigue processes below 10^6

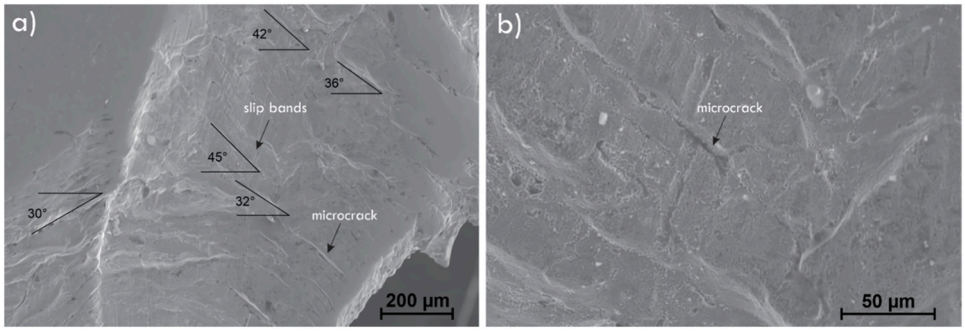

Fig. 9. Scanning electron microscopy (SEM) images of fracture regions in tensile-tested specimens: (a) necking–fracture zone of CCA1200; (b) failure zone of CCA1200.

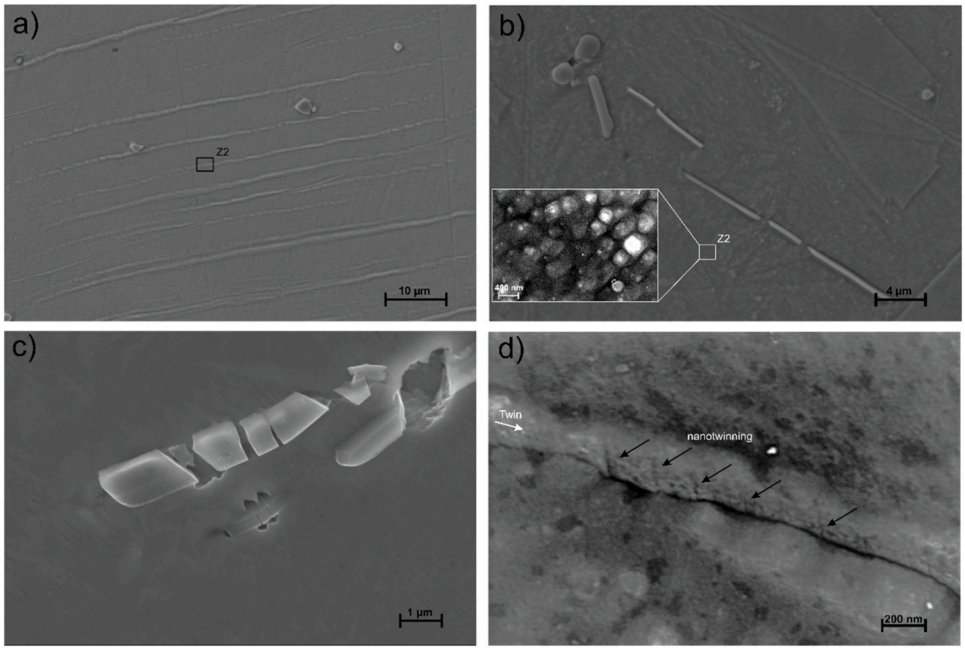

Fig. 10. Scanning electron microscopy images after the tensile test of the CCA1200 sample: a) twinning zone; b) region adjacent to the fracture surface showing magnified nanoprecipitates (Z2); c) region adjacent to the fracture surface showing magnified precipitate damage; d) nanotwinning zone (Z1) within a deformation twin.

cycles.

However, the present authors consider that the formation of FGAs can also arise from a high degree of localized plasticity prior to crack initiation, producing subgrains through intense dislocation activity, independent of a fatigue-specific condition. Fig. 11.c shows Zone Z2, located slightly farther from the fracture surface. A distorted microstructural state with severe deformation is evident, along with what appears to be an incomplete stage of subgrain formation, corresponding to a transitional state toward what is observed in Z1. Microcracks can also be identified at what seems to be the boundary of forming subgrains. These observations are consistent with those reported in [80,81], which indicate that the generation of such subgrains results from the severe accumulation of dislocations.

Fig. 12 presents the SEM–EBSD characterization of the tensile specimen after fracture. Fig. 12a shows the SEM micrograph acquired at a magnification of 991 × , in which clear evidence of deformation twinning is observed. This observation is corroborated in Fig. 12b through the IPF map, which reveals that twins are preferentially generated along the ⟨111⟩ direction. Fig. 12c shows the misorientation angle distribution, where a distinct CSL Σ3 boundary at 60° is identified, corresponding to twinning along the ⟨111⟩ direction. This finding supports the strain-hardening rate results observed in Region II (see Fig. 8), indicating that deformation twinning is a critical mechanism for achieving satisfactory performance under cryogenic impact conditions, where maximizing energy absorption is essential. Furthermore, these results are consistent with the pop-in events observed at higher load levels in the P–h curve shown in Fig. 6, which may be associated with twinning activity or a mixed deformation mechanism.

The low-temperature mechanical response obtained from Charpy impact tests is presented in Table 8. The Charpy response strongly depends on the microstructure, defects, and interstitial elements in an alloy. For example, Zhiming et al. [82] reported that in a (CoCrFeMnNi) 98C2 alloy, the absorbed impact energy was 86 J/cm^2 at –196 °C and 85 J/cm^2 at 20 °C, showing only a slight increase in energy absorption at cryogenic temperatures. However, by reducing the carbon content to (CoCrFeMnNi)99.5C0.5, the absorbed impact energy increased to 130 J/cm^2 at –196 °C and 119 J/cm^2 at 20 °C, demonstrating the dependence of impact energy absorption in multicomponent alloys on their carbon content. Moreover, when carbon was completely removed, the CoCrFeMnNi alloy exhibited absorbed impact energies of 140 J/cm^2 at –196 °C and 142 J/cm^2 at 20 °C, thereby confirming that carbon decreases impact energy absorption in multicomponent alloys.

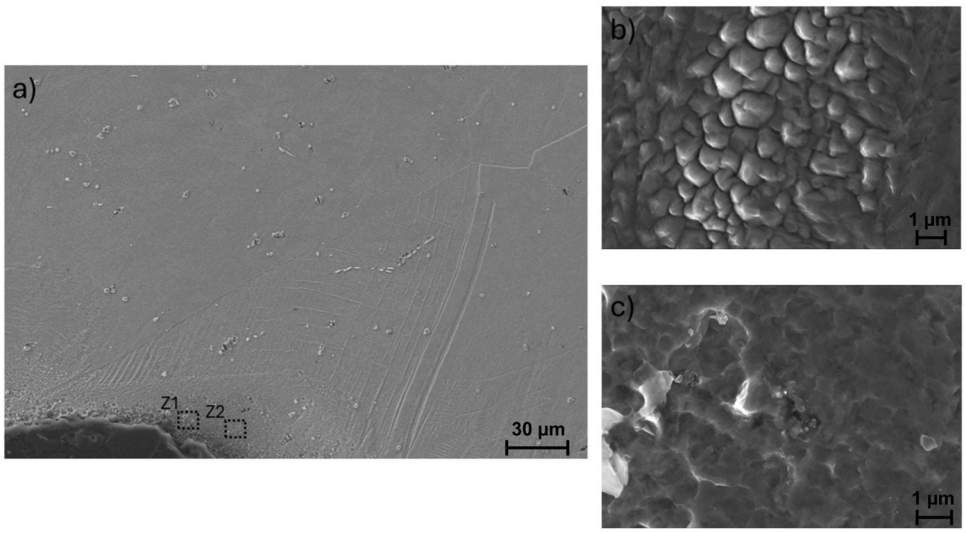

Fig. 11. Scanning electron microscopy images after the tensile test of the CCA1200 sample: a) region adjacent to the fracture surface of the CCA1200 specimen subjected to tension; b) 8810 × magnification in Zone Z1; c) 11,310 × magnification in Zone Z2.

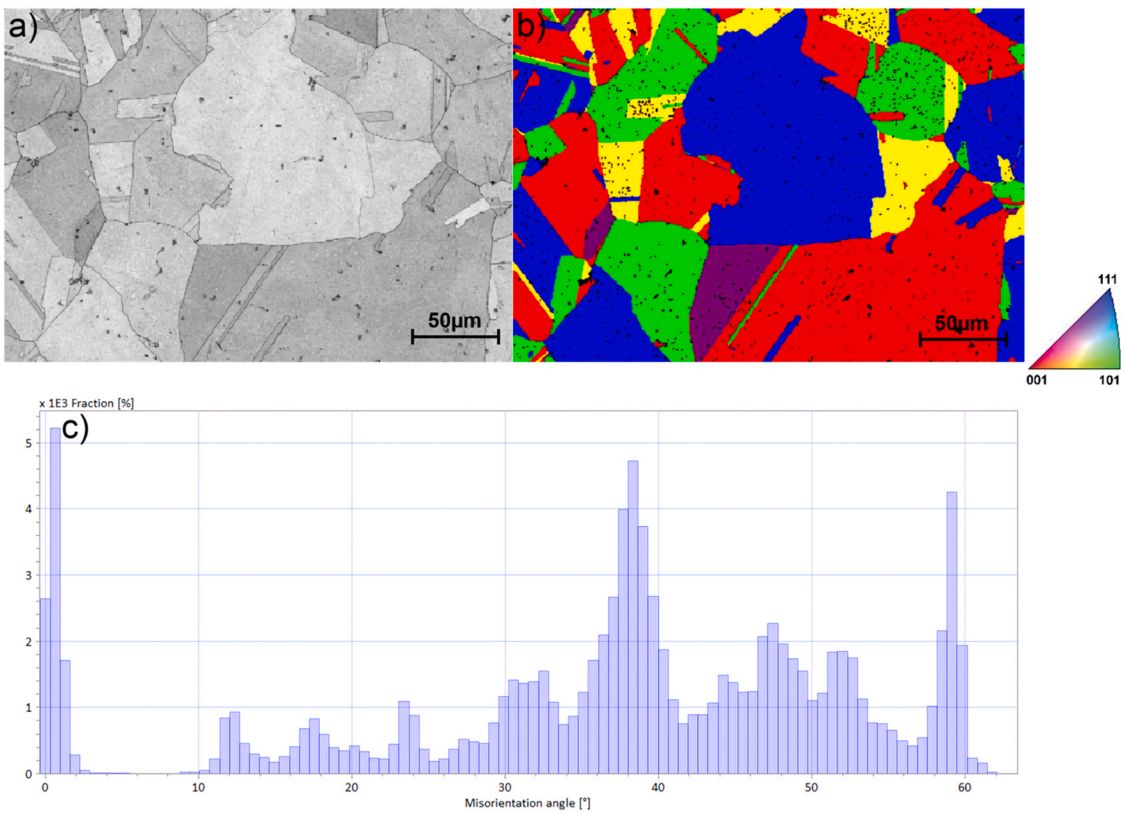

Fig. 12. EBSD analysis of specimens after tensile testing: (a) SEM image at 991 × magnification; (b) EBSD IPF map acquired in the region shown in (a); (c) Misorientation angle in the region shown in (b).

Similarly, Li et al. [83] evaluated the impact resistance of the FeCoCrNi high-entropy alloy at different heat-treatment temperatures.

The increase in energy absorption with decreasing temperature in multicomponent alloys has been reported for FCC structures [83–85] as well as in certain Mn-containing alloys [86]. This effect is primarily attributed to the activation of deformation twinning and the appropriate control of the stacking fault energy (SFE), which can decrease by 20–60 % at 77 K [87,88]. Conversely, the opposite effect occurs in metastable FCC alloys, where austenite transforms into ε or α′ phases due to excessively low SFE values at room temperatura [72,89–95]. This transformation is responsible for the loss of toughness in austenitic steels such as 304 L and 316 L [96,97], which are currently employed in cryogenic storage systems but pose a significant structural risk in applications involving the transport of energy in liquid form, such as hydrogen.

Another factor affecting energy absorption and material toughness is the presence of intermetallic phases. For example, Xia et al. [85], reported that the presence of the B2 phase within an FCC structure

Table 8
Summary of Charpy impact test results for CCA1200 alloy compared with high-entropy alloys tested under cryogenic conditions.

Alloy	Temperature	Impact toughness	Ref.
CoCrFeMnNi	27°C	177 J/cm^2	[84]
CoCrFeMnNi	-149°C	213 J/cm^2	[84]
$Al_{0.3}$CoCrFeNi	25°C	413 J/cm^2	[89]
$Al_{0.3}$CoCrFeNi	-196°C	328 J/cm^2	[89]
$AL_{0.1}$CoCrFeNi	25	420 J/cm^2	[99]
$AL_{0.1}$CoCrFeNi	-196	289 J/cm^2	[99]
Fe30Mn0.11 C	25	269 J/cm^2	[86]
Fe30Mn0.11 C	-196	372 J/cm^2	[86]
CoCrFeNi	25°C	287 J/cm^2	[85]
CoCrFeNi	-196°C	398 J/cm^2	[85]
$Al_{1.5}$CoCrFeNi	25°C	1.28 J/cm^2	[85]
$Al_{1.5}$CoCrFeNi	-196°C	0.64 J/cm^2	[85]
304 L	25°C	118 J/cm^2	[97]
304 L	-196°C	71 J/cm^2	[97]
316 L	25°C	295 J/cm^2	[96]
316 L	-196°C	181 J/cm^2	[96]
CCA1200	25°C	205 J/cm^2	This work
CCA1200	-196°C	226 J/cm^2	This work

resulted in extremely low levels of energy absorption, reaching only 1.28 J/cm^2 at room temperature and 0.64 J/cm^2 at 77 K. These findings highlight the critical need for microstructural control and the regulation of intermetallic content in multicomponent alloys.

Based on the preceding discussion, the CCA1200 alloy presented in this work exhibited a significant performance in impact tests. Considering that its fabrication was carried out using scrap as the primary feedstock, which introduced carbon, and that its microstructure did not achieve complete solubilization, resulting in the presence of σ phase and TiC precipitates, the absorbed impact energy reached 205 J/cm^2 at room temperature and 226 J/cm^2 at 77 K. These results clearly demonstrate that energy absorption increases with decreasing temperature. Furthermore, Fig. 13.a) shows that the CCA1200 alloy evaluated in the present work falls within the upper range of the overall toughness reported for FCC-structured high-entropy alloys at 77 K, even surpassing Mn-based steels exhibiting TWIP mechanisms, consistent with the findings reported by Yoon et al. [98].

Although the obtained values are lower than those reported for other multicomponent alloys (see Table 8), it must be emphasized that high-entropy or complex concentrated alloys are typically produced from high-purity elements, which substantially increases costs while minimizing defect formation. Therefore, this study demonstrates that multicomponent alloys can be successfully fabricated from recycled scrap while still achieving excellent mechanical performance, thereby reducing production costs and opening pathways for large-scale manufacturing.

When comparing the CCA1200 alloy with conventional cryogenic storage alloys such as austenitic stainless steels 304 L and 316 L, it is observed that the absorbed impact energy at cryogenic temperatures is higher by 218.31 % and 24.86 %, respectively. This can be seen in detail in Fig. 13(b), where the CCA1200 alloy is compared with high-performance commercial austenitic alloys such as 304 L and 316 L, as well as multicomponent alloys fabricated from high-purity elemental feedstocks.

The microstructural changes after Charpy impact testing can be visualized in Fig. 14 through the IPF maps. A clear twinning effect is observed, which becomes more pronounced with decreasing temperature. In Fig. 14.a, the formation of mechanical twins with preferential orientation along the {111} and {001} systems can be seen, which is expected for mechanical twinning in austenitic alloys. However, when compared with the microstructural response of the specimen tested at 77 K (Fig. 14.b), a microstructure with a high density of twins and severe grain subdivision due to mechanical twinning is observed. This microstructural refinement enables high energy absorption and corroborates the 10.24 % increase in absorbed energy measured for the CCA1200 alloy tested at 77 K. Using Eq. 7, the calculation of the SFE at 77 K for the CCA1200 alloy yielded a value of 33.24 mJ/m^2, which could explain the higher density of active twinning.

The fracture surfaces of the specimens tested by the Charpy method are shown in Fig 15. The fracture zones are predominantly characterized by equiaxed dimples in all samples, which is typical of ductile failure, with patterns similar to those reported in [88]. Elongated and parabolic dimples were also observed, indicative of shear-related effects. In Fig 15. a, corresponding to the specimen tested at –196 °C, isolated particles can be observed within some dimples. These particles are likely associated with the σ phase, a stable precipitate at 1200 °C according to the phase diagram of the CCA1200 alloy. The average dimple size in this sample was measured at 26 μm. In Fig 15.b, dimples with an average size of 19 μm are observed, without the presence of metallic particles. The smaller dimple size suggests a lower energy absorption capacity, which is consistent with the impact toughness results obtained for both CCA1200 specimens.

4. Conclusion

The design of a complex concentrated austenitic alloy with an austenitic matrix and strengthening mechanisms based on precipitates and TWIP was supported by multicategorical phase prediction using machine learning combined with CALPHAD, and validated through SEM, EBSD, and XRD. The main results obtained were:

- The strong predictive capability of phase formation in multicomponent systems using the multicategorical machine learning prediction

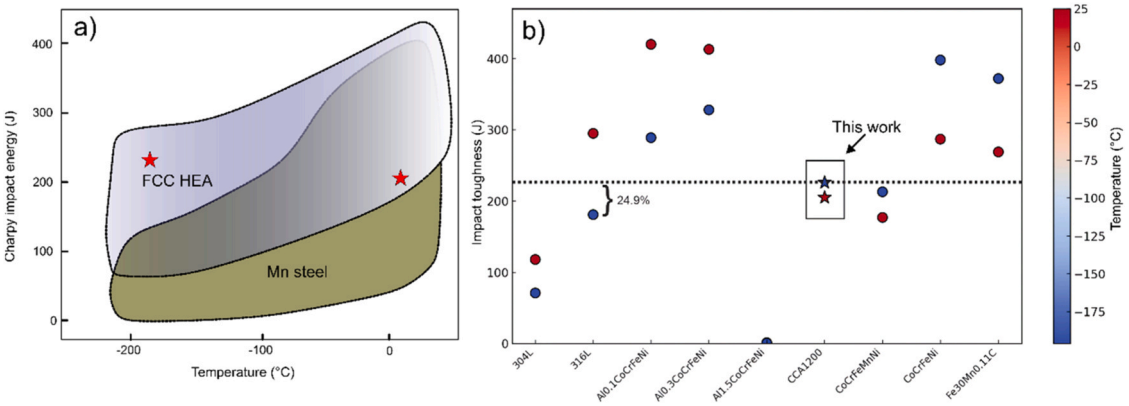

Fig. 13. a) Impact toughness comparison of the CCA1200 alloy with FCC High entropy alloys and Mn steel; b) Commercial austenitic stainless steels and High entropy alloys.

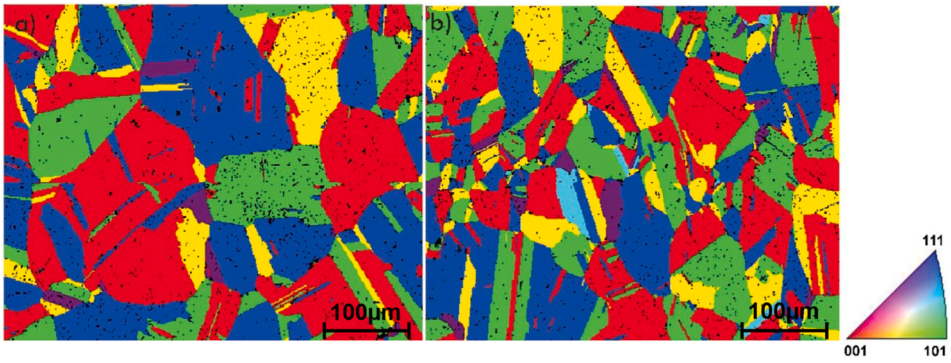

Fig. 14. EBSD IPF maps of specimens subjected to Charpy impact tests: (a) specimen tested at room temperature; (b) specimen tested at 77 K.

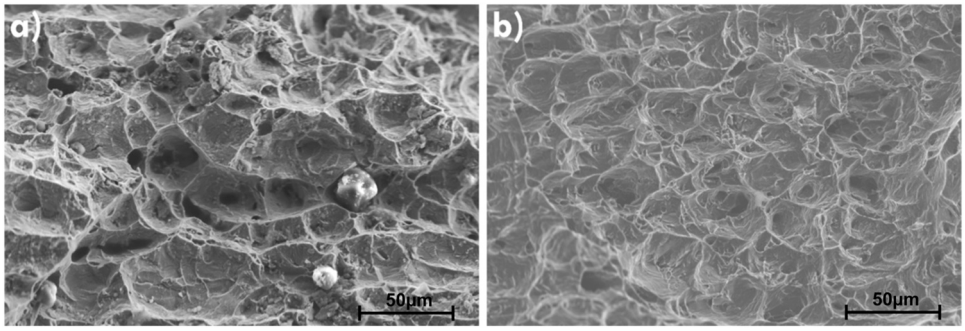

Fig. 15. Scanning electron microscopy (SEM) characterization of the fracture surfaces of Charpy-tested specimens at cryogenic and room temperatures: a) CCA1200 tested at 77 K; b) CCA1200 tested at room temperature.

method is confirmed. It is necessary to further investigate the integration of the atomic packing misfit factor as a descriptor to potentially improve predictive performance and surpass the current accuracy threshold of 77 %.

- The developed complex concentrated alloy exhibited a high strain-hardening capability, predominantly governed by mechanical twinning and precipitation strengthening of the $L1_2$ phase. Moreover, a strength–ductility product of 40.1 GPa% was achieved, resulting from the exceptional ductility of 81.46 %, despite the presence of a 1.49 wt% fraction of the σ phase.
- The nanoindentation and nanocreep results indicate a strong interaction between dislocations, nanoprecipitates, and nanoscale twinning, as evidenced by the strain-rate–versus-time response and the pop-in events in the P–h curve. Owing to this complex interaction, one of the highest n-values reported for multicomponent alloys tested under nanoindentation at loads below 1000 μN was obtained, which may be associated with the combined strengthening effects of precipitation hardening and nanometer-scale twinning.
- The FE-SEM results in the region adjacent to the fracture revealed the presence of nanograins generated by severe localized plastic deformation. This phenomenon has been previously reported in alloys subjected to high-cycle fatigue conditions; however, this is the first evidence of such grain refinement occurring in high-entropy alloys under static loading. The formation of these fine-grained areas is attributed to the development of subgrains resulting from the intense accumulation of dislocations in the crack-adjacent region.
- The energy absorption results obtained for the complex concentrated alloy show a 10.2 % increase when the temperature is reduced to 77 K compared to room temperature. This indicates that the ductile-to-brittle transition was successfully suppressed in the alloy, which may be associated with the severe mechanical twinning observed at 77 K, significantly higher than that found in specimens tested at room temperature. Furthermore, at 77 K, the alloy exhibited an energy absorption 24.86 % higher than that of 316 L stainless steel, which is commonly used in cryogenic storage systems such as liquid hydrogen and liquefied petroleum gas, thereby highlighting its potential applications in the energy sector.

CRediT authorship contribution statement

Juan Pablo Sanhueza: Writing – review & editing, Software, Resources. **Angelo Oñate:** Writing – review & editing, Writing – original draft, Visualization, Supervision, Software, Methodology, Investigation, Formal analysis, Data curation, Conceptualization. **Abdul Herrim Seidou:** Methodology. **Víctor Tuninetti:** Writing – review & editing, Methodology. **Carlos Lanziotti:** Writing – review & editing, Resources, Methodology. **Diego Wackerling:** Software. **David Rojas:** Resources.

Declaration of Competing Interest

The authors declare that they have no known competing financial interests or personal relationships that could have appeared to influence the work reported in this paper.

Acknowledgements

Angelo Oñate gratefully acknowledges the VRID Initiation Project, code 2025001319INI, granted by the University of Concepcion

References

[1] Y.H. Zhou, et al., A strong-yet-ductile high-entropy alloy in a broad temperature range from cryogenic to elevated temperatures, Acta Mater. 268 (Apr. 2024) 119770, https://doi.org/10.1016/j.actamat.2024.119770.
[2] Q. Wu, et al., Cryogenic dynamic-mechanical property and microstructure of a selective laser melting FeCoNiCrMo0.2 high-entropy alloy, Mater. Today Commun. 39 (Jun. 2024) 108928, https://doi.org/10.1016/j.mtcomm.2024.108928.

[3] Y.H. Jo, Y.T. Choi, D.G. Kim, J. Han, S. Lee, Toughness behavior and deformation mechanisms in FCC-based Fe45Co30Cr10V10Ni5-xMnx high-entropy alloys: Insights from instrumented Charpy impact tests, J. Mater. Res. Technol. 30 (May 2024) 1758–1767, https://doi.org/10.1016/j.jmrt.2024.03.211.

[4] L. Sun, et al., Local chemical order enables an ultrastrong and ductile high-entropy alloy in a cryogenic environment, Sci. Adv. 10 (48) (Nov. 2024), https://doi.org/10.1126/sciadv.adq6398.

[5] Z. An, et al., Achieving superior combined cryogenic strength and ductility in a high-entropy alloy via the synergy of low stacking fault energy and multiscale heterostructure, Scr. Mater. 239 (Jan. 2024) 115809, https://doi.org/10.1016/j.scriptamat.2023.115809.

[6] K. Jiang, et al., Dynamic mechanical responses of the Al0·1CoCrFeNi high entropy alloy at cryogenic temperature, Mater. Sci. Eng. A 797 (Oct. 2020) 140125, https://doi.org/10.1016/j.msea.2020.140125.

[7] J. Wang, P.A. Webley, T.J. Hughes, Thermodynamic modelling of low fill levels in cryogenic storage tanks for application to liquid hydrogen maritime transport, Appl. Therm. Eng. 256 (Nov. 2024) 124054, https://doi.org/10.1016/j.applthermaleng.2024.124054.

[8] J. Kim, et al., Technical feasibility of large-scale transportable liquid hydrogen export terminal, Int J. Hydrog. Energy 66 (May 2024) 499–511, https://doi.org/10.1016/j.ijhydene.2024.03.343.

[9] R. Fussik, G. Egels, W. Theisen, S. Weber, Stacking fault energy in relation to hydrogen environment embrittlement of metastable austenitic stainless crni-steels, Metals (Basel) 11 (8) (Jul. 2021) 1170, https://doi.org/10.3390/met11081170.

[10] T. Michler, J. Naumann, M.P. Balogh, Hydrogen environment embrittlement of solution treated Fe–Cr–Ni super alloys, Mater. Sci. Eng. A 607 (Jun. 2014) 71–80, https://doi.org/10.1016/j.msea.2014.03.134.

[11] S. Chen, M. Zhao, L. Rong, Hydrogen-induced cracking behavior of twin boundary in γ′ phase strengthened Fe–Ni based austenitic alloys, Mater. Sci. Eng. A 561 (Jan. 2013) 7–12, https://doi.org/10.1016/j.msea.2012.10.069.

[12] A. Fukunaga, Hydrogen embrittlement behaviors during SSRT tests in gaseous hydrogen for cold-worked type 316 austenitic stainless steel and iron-based superalloy A286 used in hydrogen refueling station, Eng. Fail Anal. 160 (Jun. 2024) 108158, https://doi.org/10.1016/j.engfailanal.2024.108158.

[13] L. Zhang, M. Wen, M. Imade, S. Fukuyama, K. Yokogawa, Effect of nickel equivalent on hydrogen gas embrittlement of austenitic stainless steels based on type 316 at low temperatures, Acta Mater. 56 (14) (Aug. 2008) 3414–3421, https://doi.org/10.1016/j.actamat.2008.03.022.

[14] M. Jiang, et al., High cryogenic ductility of the high-entropy alloy CoCrFeNiAl0.1Ti0.05 at 77 K, J. Appl. Phys. 134 (18) (Nov. 2023), https://doi.org/10.1063/5.0172237.

[15] D. Zhou, C. Shi, C. Wang, R. Sheng, W. Li, Y. Tong, Tensile properties of a non-equiatomic Ni–Co–V medium entropy alloy at cryogenic temperature, Metals (Basel) 14 (5) (May 2024) 590, https://doi.org/10.3390/met14050590.

[16] M. Cabrera, Y. Oropesa, J.P. Sanhueza, V. Tuninetti, A. Oñate, Multicomponent alloys design and mechanical response: from high entropy alloys to complex concentrated alloys, Mater. Sci. Eng. R Rep. 161 (Dec. 2024) 100853, https://doi.org/10.1016/J.MSER.2024.100853.

[17] A. Oñate, J.P. Sanhueza, J. Ramirez, C. Medina, M.F. Melendrez, D. Rojas, Design of Fe36.29Cr28.9Ni26.15Cu4.17Ti1.67V2.48C0.46 HEA using a new criterion based on VEC: microstructural study and multiscale mechanical response, Mater. Today Commun. 35 (Jun. 2023) 105681, https://doi.org/10.1016/J.MTCOMM.2023.105681.

[18] A. Oñate, et al., Supervised machine learning-based multi-class phase prediction in high-entropy alloys using robust databases, J. Alloy. Compd. 962 (Nov. 2023) 171224, https://doi.org/10.1016/J.JALLCOM.2023.171224.

[19] A. Oñate, et al., New analytical parameters for B2 phase prediction as a complement to multiclass phase prediction using machine learning in multicomponent alloys: a computational approach with experimental validation, J. Alloy. Compd. 1022 (Apr. 2025) 179950, https://doi.org/10.1016/j.jallcom.2025.179950.

[20] Y. Yan, X. Hu, Y. Liao, Y. Zhou, W. He, T. Zhou, Recent machine learning-driven investigations into high entropy alloys: a comprehensive review, J. Alloy. Compd. 1010 (Jan. 2025) 177823, https://doi.org/10.1016/j.jallcom.2024.177823.

[21] F. Yang, L. Dong, L. Cai, X. Hu, F. Fang, Mechanical properties of FeMnCoCr high entropy alloy alloyed with C/Si at low temperatures, J. Alloy. Compd. 859 (Apr. 2021) 157876, https://doi.org/10.1016/J.JALLCOM.2020.157876.

[22] M.S. Rizi, H. Minouei, B.J. Lee, H. Pouraliakbar, M.R. Toroghinejad, S.I. Hong, Hierarchically activated deformation mechanisms to form ultra-fine grain microstructure in carbon containing FeMnCoCr twinning induced plasticity high entropy alloy, Mater. Sci. Eng. A 824 (Sep. 2021) 141803, https://doi.org/10.1016/J.MSEA.2021.141803.

[23] X. Tian, Y. Zhang, Effect of Si content on the stacking fault energy in γ-Fe–Mn–Si–C alloys: Part I. X-ray diffraction line profile analysis, Mater. Sci. Eng. A 516 (1–2) (Aug. 2009) 73–77, https://doi.org/10.1016/J.MSEA.2009.02.031.

[24] G.B. Olson, M. Cohen, A general mechanism of martensitic nucleation: Part I. General concepts and the FCC → HCP transformation, Metall. Trans. A 7 (12) (Dec. 1976) 1897–1904, https://doi.org/10.1007/BF02659822/METRICS.

[25] W.C. Oliver, G.M. Pharr, An improved technique for determining hardness and elastic modulus using load and displacement sensing indentation experiments, J. Mater. Res. 7 (6) (Jun. 1992) 1564–1583, https://doi.org/10.1557/JMR.1992.1564.

[26] W.C. Oliver, G.M. Pharr, An improved technique for determining hardness and elastic modulus using load and displacement sensing indentation experiments, 1992 7:6, J. Mater. Res. 7 (6) (Jan. 2011) 1564–1583, https://doi.org/10.1557/JMR.1992.1564.

[27] P.F. Zhou, D.H. Xiao, G. Li, M. Song, Nanoindentation creep behavior of CoCrFeNiMn high-entropy alloy under different high-pressure torsion deformations, J. Mater. Eng. Perform. 28 (5) (May 2019) 2620–2629, https://doi.org/10.1007/S11665-019-04092-1/TABLES/3.

[28] Z.M. Jiao, M.Y. Chu, H.J. Yang, Z.H. Wang, and J.W. Qiao, "Nanoindentation characterised plastic deformation of a Al0.5CoCrFeNi high entropy alloy," https://doi.org/10.1179/1743284715Y.0000000048, vol. 31, no. 10, pp. 1244–1249, Jul. 2015, doi: 10.1179/1743284715Y.0000000048.

[29] W.C. Oliver, G.M. Pharr, Measurement of hardness and elastic modulus by instrumented indentation: advances in understanding and refinements to methodology, J. Mater. Res. 19 (1) (2004) 3–20, https://doi.org/10.1557/JMR.2004.19.1.3.

[30] J.E. Jakes, D.S. Stone, Best practices for quasistatic berkovich nanoindentation of Wood Cell Walls, Forests 12 (12) (Dec. 2021) 1696, https://doi.org/10.3390/F12121696.

[31] M.G. Poletti, L. Battezzati, Electronic and thermodynamic criteria for the occurrence of high entropy alloys in metallic systems, Acta Mater. 75 (Aug. 2014) 297–306, https://doi.org/10.1016/j.actamat.2014.04.033.

[32] Y. Dong, Y. Lu, L. Jiang, T. Wang, T. Li, Effects of electro-negativity on the stability of topologically close-packed phase in high entropy alloys, Intermetallics (Barking) 52 (Sep. 2014) 105–109, https://doi.org/10.1016/J.INTERMET.2014.04.001.

[33] Zhijun Wangab, Weifeng Qiuc, Yong Yanga, C.T. Liu, Atomic-size and lattice-distortion effects in newly developed high-entropy alloys with multiple principal elements, Intermetallics(Barking) 64 (Sep. 2015) 63–69, https://doi.org/10.1016/J.INTERMET.2015.04.014.

[34] Z. Wang, Y. Huang, Y. Yang, J. Wang, C.T. Liu, Atomic-size effect and solid solubility of multicomponent alloys, Scr. Mater. 94 (Jan. 2015) 28–31, https://doi.org/10.1016/j.scriptamat.2014.09.010.

[35] M.-H. Tsai, K.-C. Chang, J.-H. Li, R.-C. Tsai, A.-H. Cheng, A second criterion for sigma phase formation in high-entropy alloys, Mater. Res Lett. 4 (2) (Oct. 2016) 90–95.

[36] A. Oñate, et al., Sigma phase stabilization by Nb doping in a new high-entropy alloy in the FeCrMnNiCu system: a study of phase prediction and nanomechanical response, Metals 14 (1) (Jan. 2024) 74, https://doi.org/10.3390/MET14010074.

[37] B. Han, et al., Composition evolution of gamma prime nanoparticles in the Ti-doped CoFeCrNi high entropy alloy, Scr. Mater. 148 (Apr. 2018) 42–46, https://doi.org/10.1016/J.SCRIPTAMAT.2018.01.025.

[38] J. Fadok, Advanced gas turbine materials, design and technology, Adv. Power Plant Mater. Des. Technol. (2010) 3–31, https://doi.org/10.1533/9781845699468.1.3.

[39] S. Rosen, P.G. Sprang, The structure of the γ'-phase in nickel-base superalloys, Adv. XRay Anal. (1966) 131–141, https://doi.org/10.1007/978-1-4684-7633-0_11.

[40] L. Finet, V.A. Esin, V. Maurel, L. Nazé, Composition and temperature stability of η and δ phases for future nickel-base superalloys for turbine disks application, Miner. Met. Mater. Ser. (2020) 112–121, https://doi.org/10.1007/978-3-030-51834-9_11/TABLES/1.

[41] A. Di Gianfrancesco"Alloy 263," Materials for Ultra-Supercritical and Advanced Ultra-Supercritical Power Plants, pp. 571–599Jan. 2017, 57159910.1016/B978-0-08-100552-1.00017-8.

[42] M. Premkumar, K.S. Prasad, A.K. Singh, Structure and stability of the B2 phase in Ti–25Al–25Zr alloy, Intermetallics (Barking) 17 (3) (Mar. 2009) 142–145, https://doi.org/10.1016/J.INTERMET.2008.10.009.

[43] K.A. Gschneidner, et al., Influence of the electronic structure on the ductile behavior of B2 CsCl-type AB intermetallics, Acta Mater. 57 (19) (Nov. 2009) 5876–5881, https://doi.org/10.1016/J.ACTAMAT.2009.08.012.

[44] R.E. Smallman, A.H.W. Ngan, Plastic deformation and dislocation behaviour, Mod. Phys. Metall. (2014) 357–414, https://doi.org/10.1016/B978-0-08-098204-5.00009-2.

[45] E.O. Hall and S.H. Algie, "The Sigma Phase," https://doi.org/10.1179/mtlr.1966.11.1.61, vol. 11, no. 1, pp. 61–88, 2013, doi: 10.1179/MTLR.1966.11.1.61.

[46] Q. Yang, D. Yan, Y. Zhang, K. Gan, Z. Li, Formation mechanisms of two types of sigma phases and the effects on mechanical behavior in a quaternary metastable high-entropy alloy, Mater. Sci. Eng. A 894 (Mar. 2024) 146224, https://doi.org/10.1016/J.MSEA.2024.146224.

[47] T.X. Bai, et al., Fine regulation of sigma phase achieves excellent mechanical properties in Co-free CrFeNiSi0.2 medium entropy alloy, J. Mater. Res. Technol. 36 (May 2025) 9274–9282, https://doi.org/10.1016/J.JMRT.2025.05.151.

[48] M.Y. He, Y.F. Shen, N. Jia, P.K. Liaw, C and N doping in high-entropy alloys: a pathway to achieve desired strength-ductility synergy, Appl. Mater. Today 25 (Dec. 2021) 101162, https://doi.org/10.1016/J.APMT.2021.101162.

[49] A. Mozafari, B. Fu, D. Chalapathi, H. Abdolvand, Characterization of IN738LC using in situ nanoindentation and crystal plasticity modeling, Mater. Des. 257 (Sep. 2025) 114378, https://doi.org/10.1016/J.MATDES.2025.114378.

[50] T. Ohmura, M. Wakeda, Pop-in phenomenon as a fundamental plasticity probed by nanoindentation technique, Materials 14 (8) (Apr. 2021) 1879, https://doi.org/10.3390/MA14081879.

[51] J.A. Castañeda, O.A. Zambrano, R.M. Souza, J.J. Coronado, S.A. Rodriguez, Unveiling the mechanism of cyclic indentation in a Fe–Mn–Al–C alloy, 56:11, Metall. Mater. Trans. A 56 (11) (Aug. 2025) 4913–4929, https://doi.org/10.1007/S11661-025-07923-0.

[52] X.X. Ye, et al., Study of twinning behavior of powder metallurgy Ti-Si alloy by interrupted in-situ tensile tests, Mater. Sci. Eng. A 679 (Jan. 2017) 543–553, https://doi.org/10.1016/J.MSEA.2016.10.070.

[53] M. Yang, et al., Fine-grained TWIP steel prepared by powder metallurgy, J. Phys. Conf. Ser. 2951 (1) (Feb. 2025) 012023, https://doi.org/10.1088/1742-6596/2951/1/012023.

[54] M.B. Jabłońska, K. Jasiak, K. Kowalczyk, M. Skwarski, K. Rodak, Z. Gronostajski, The influence of the heat generation during deformation on the mechanical properties and microstructure of the selected TWIP steels, Int. J. Mater. Form. 16 (3) (May 2023) 1–17, https://doi.org/10.1007/S12289-023-01753-4/FIGURES/20.

[55] Q. Fan, K. Gan, D. Yan, Z. Li, Nanoindentation creep behavior of diverse microstructures in a pre-strained interstitial high-entropy alloy by high-throughput mapping, Mater. Sci. Eng. A 856 (Oct. 2022) 143988, https://doi.org/10.1016/J.MSEA.2022.143988.

[56] Q. Shen, X. Kong, X. Chen, Significant transitions of microstructure and mechanical properties in additively manufactured Al–Co–Cr–Fe–Ni high-entropy alloy under heat treatment, Mater. Sci. Eng. A 815 (May 2021) 141257, https://doi.org/10.1016/J.MSEA.2021.141257.

[57] J.Y. Aguilar-Hurtado, et al., Experimental and computational analysis of stacking fault energy in B-doped Fe50−XMn30Co10Cr10BX multi-principal elements alloys, J. Alloy. Compd. 969 (Dec. 2023) 172428, https://doi.org/10.1016/J.JALLCOM.2023.172428.

[58] W. Woo, et al., Stacking fault energy analyses of additively manufactured stainless steel 316L and CrCoNi medium entropy alloy using in situ neutron diffraction, Sci. Rep. 2020 10 (1) (Jan. 2020) 1350, https://doi.org/10.1038/s41598-020-58273-3.

[59] G.Z. Voyiadjis, M. Yaghoobi, Review of nanoindentation size effect: experiments and atomistic simulation, Crystals 7 (10) (Oct. 2017) 321, https://doi.org/10.3390/CRYST7100321.

[60] K. Han, et al., Nanoindentation creep behavior of high entropy superalloy with γ/γ' microstructure under various loads and temperatures, J. Alloy. Compd. 1031 (Jun. 2025) 180985, https://doi.org/10.1016/J.JALLCOM.2025.180985.

[61] Y. Ma, Y.H. Feng, T.T. Debela, G.J. Peng, T.H. Zhang, Nanoindentation study on the creep characteristics of high-entropy alloy films: fcc versus bcc structures, Int. J. Refract Met. Hard Mater. 54 (Jan. 2016) 395–400, https://doi.org/10.1016/J.IJRMHM.2015.08.010.

[62] B. Wei, T. Zhang, W. Li, D. Xing, L. Zhang, Y. Wang, Indentation creep behavior in Ce-based bulk metallic glasses at room temperature, Mater. Trans. 46 (12) (Dec. 2005) 2959–2962, https://doi.org/10.2320/MATERTRANS.46.2959.

[63] P.F. Yu, et al., Room-temperature creep resistance of Co-based metallic glasses, Scr. Mater. 90–91 (1) (Nov. 2014) 45–48, https://doi.org/10.1016/J.SCRIPTAMAT.2014.07.013.

[64] A. Sharma, et al., High-temperature nanoindentation creep studies on castable and sintered nanostructured low-activation ferritic-martensitic alloys, J. Nucl. Mater. 611 (Jun. 2025) 155804, https://doi.org/10.1016/J.JNUCMAT.2025.155804.

[65] M. Sadeghilaridjani, S. Mukherjee, High-temperature nano-indentation creep behavior of multi-principal element alloys under static and dynamic loads, Metals 10 (2) (Feb. 2020) 250, https://doi.org/10.3390/MET10020250.

[66] Z. Wang, X.W. Yang, Q. Zhang, J.W. Qiao, Nanoindentation creep behavior of hexagonal close-packed high-entropy alloys, Met. Mater. Int. 30 (9) (Mar. 2024) 2433–2439, https://doi.org/10.1007/S12540-024-01655-3.

[67] J. Wang, C. Yang, Y. Liu, Y. Li, Y. Xiong, Using nanoindentation to characterize the mechanical and creep properties of shale: load and loading strain rate effects, ACS Omega 7 (16) (Apr. 2022) 14317–14331, https://doi.org/10.1021/ACSOMEGA.2C01190/ASSET/IMAGES/LARGE/AO2C01190_0015.JPEG.

[68] Q. Fan, K. Gan, D. Yan, Z. Li, Nanoindentation creep behavior of diverse microstructures in a pre-strained interstitial high-entropy alloy by high-throughput mapping, Mater. Sci. Eng. A 856 (Oct. 2022) 143988, https://doi.org/10.1016/J.MSEA.2022.143988.

[69] L. Zeng, L. Zeng, R. Gao, C. You, B. Liu, Achieving ultra-high strength in a face-centered-cubic FeCrCoNi high entropy alloy through dense nanotwins bundles structure prepared by cryo-rolling, Intermetallics (Barking) 148 (Sep. 2022) 107638, https://doi.org/10.1016/J.INTERMET.2022.107638.

[70] X. Pan, G. Qian, Y. Hong, Nanograin formation in dimple ridges due to local severe-plastic-deformation during ductile fracture, Scr. Mater. 194 (Mar. 2021) 113631, https://doi.org/10.1016/J.SCRIPTAMAT.2020.113631.

[71] J.Y. He, et al., A precipitation-hardened high-entropy alloy with outstanding tensile properties, Acta Mater. 102 (Jan. 2016) 187–196, https://doi.org/10.1016/J.ACTAMAT.2015.08.076.

[72] W. Li, D. Xie, D. Li, Y. Zhang, Y. Gao, P.K. Liaw, Mechanical behavior of high-entropy alloys, Prog. Mater. Sci. 118 (May 2021) 100777, https://doi.org/10.1016/J.PMATSCI.2021.100777.

[73] W.S. Park, M.S. Chun, M.S. Han, M.H. Kim, J.M. Lee, Comparative study on mechanical behavior of low temperature application materials for ships and offshore structures: part I—experimental investigations, Mater. Sci. Eng. A 528 (18) (Jul. 2011) 5790–5803, https://doi.org/10.1016/J.MSEA.2011.04.032.

[74] N. Kumar, et al., High strain-rate compressive deformation behavior of the Al0.1CrFeCoNi high entropy alloy, Mater. Des. 86 (Dec. 2015) 598–602, https://doi.org/10.1016/J.MATDES.2015.07.161.

[75] W.P. Li, X.G. Wang, B. Liu, Q.H. Fang, C. Jiang, Fracture mechanisms of a Mo alloyed CoCrFeNi high entropy alloy: in-situ SEM investigation, Mater. Sci. Eng. A 723 (Apr. 2018) 79–88, https://doi.org/10.1016/J.MSEA.2018.03.032.

[76] Y.Morris Wang, et al., Defective twin boundaries in nanotwinned metals, 12:8, Nat. Mater. 12 (8) (May 2013) 697–702, https://doi.org/10.1038/nmat3646.

[77] L. Sun, X. He, J. Lu, Nanotwinned and hierarchical nanotwinned metals: a review of experimental, computational and theoretical efforts, npj Comput. Mater. 2018 4 (1) (Feb. 2018) 6, https://doi.org/10.1038/s41524-018-0062-2.

[78] P. Xie, et al., A nanotwinned surface layer generated by high strain-rate deformation in a TRIP steel, Mater. Des. 80 (Sep. 2015) 144–151, https://doi.org/10.1016/J.MATDES.2015.05.017.

[79] G. Huang, B. Li, Y. Chen, F. Xuan, Nanotwining induced by tensile fatigue and dynamic impact of laser powder bed fusion additively manufactured CoCrFeNi high-entropy alloy, J. Mater. Sci. Technol. 183 (Jun. 2024) 241–257, https://doi.org/10.1016/J.JMST.2023.10.028.

[80] J. Li, et al., Crack-tip plasticity mediated grain refinement and its resisting effect on the fatigue short crack growth, Int. J. Plast. 181 (Oct. 2024) 104102, https://doi.org/10.1016/J.IJPLAS.2024.104102.

[81] B. Zhu, et al., Unveiling the underlying mechanism of forming edge cracks upon high strain-rate rolling of magnesium alloy, J. Mater. Sci. Technol. 50 (Aug. 2020) 59–65, https://doi.org/10.1016/J.JMST.2020.03.006.

[82] Zhiming composite, Guo, et al., Effect of carbon content on cryogenic mechanical properties of CoCrFeMnNi high entropy alloy, IOP Conf. Ser. Mater. Sci. Eng. 1014 (1) (Jan. 2021) 012050, https://doi.org/10.1088/1757-899X/1014/1/012050.

[83] D. Lin, L. Xu, H. Jing, Y. Han, L. Zhao, F. Minami, Effects of annealing on the structure and mechanical properties of FeCoCrNi high-entropy alloy fabricated via selective laser melting, Addit. Manuf. 32 (Mar. 2020) 101058, https://doi.org/10.1016/J.ADDMA.2020.101058.

[84] J.H. Kim, K.R. Lim, J.W. Won, Y.S. Na, H.-S. Kim, Mechanical properties and deformation twinning behavior of as-cast CoCrFeMnNi high-entropy alloy at low and high temperatures, Mater. Sci. Eng. A 712 (Jan. 2018) 108–113, https://doi.org/10.1016/j.msea.2017.11.081.

[85] S.Q. Xia, M.C. Gao, Y. Zhang, Abnormal temperature dependence of impact toughness in Al CoCrFeNi system high entropy alloys, Mater. Chem. Phys. 210 (May 2018) 213–221, https://doi.org/10.1016/j.matchemphys.2017.06.021.

[86] Y. Wang, et al., Cryogenic toughness in a low-cost austenitic steel, Commun. Mater. 2 (1) (Apr. 2021) 44, https://doi.org/10.1038/s43246-021-00149-8.

[87] S. Curtze, V.-T. Kuokkala, Dependence of tensile deformation behavior of TWIP steels on stacking fault energy, temperature and strain rate, Acta Mater. 58 (15) (Sep. 2010) 5129–5141, https://doi.org/10.1016/j.actamat.2010.05.049.

[88] W. Jiang, et al., Charpy impact behavior and deformation mechanisms of Cr26Mn20Fe20Co20Ni14 high-entropy alloy at ambient and cryogenic temperatures, Mater. Sci. Eng. A 837 (Mar. 2022) 142735, https://doi.org/10.1016/J.MSEA.2022.142735.

[89] D. Li, Y. Zhang, The ultrahigh charpy impact toughness of forged AlxCoCrFeNi high entropy alloys at room and cryogenic temperatures, Intermetallics (Barking) 70 (Mar. 2016) 24–28, https://doi.org/10.1016/j.intermet.2015.11.002.

[90] J.W. Bae, et al., Exceptional phase-transformation strengthening of ferrous medium-entropy alloys at cryogenic temperatures, Acta Mater. 161 (Dec. 2018) 388–399, https://doi.org/10.1016/j.actamat.2018.09.057.

[91] J. Li, et al., Cryogenic impact property of a high-strength-ductility 304L stainless steel with heterogeneous lamella structure, J. Mater. Res. Technol. 24 (May 2023) 1401–1409, https://doi.org/10.1016/j.jmrt.2023.03.081.

[92] J. Li, et al., Effects of geometric dimension and grain size on impact properties of 316L stainless steel, Mater. Lett. 284 (Feb. 2021) 128908, https://doi.org/10.1016/j.matlet.2020.128908.

[93] G.-H. Lee, et al., Phase transformation and deformation mechanisms of 304L stainless steel under tensile and charpy impact testing at varying temperatures, Crystals (Basel) 15 (4) (Apr. 2025) 360, https://doi.org/10.3390/cryst15040360.

[94] M.S. Mehranpour, et al., Exceptional strength-ductility synergy in the novel metastable FeCoCrNiVSi high-entropy alloys via tuning the grain size dependency of the transformation-induced plasticity effect, Int. J. Plast. 182 (Nov. 2024) 104115, https://doi.org/10.1016/j.ijplas.2024.104115.

[95] R.R. Eleti, M. Klimova, M. Tikhonovsky, N. Stepanov, S. Zherebtsov, Exceptionally high strain-hardening and ductility due to transformation induced plasticity effect in Ti-rich high-entropy alloys, Sci. Rep. 10 (1) (Aug. 2020) 1–8, https://doi.org/10.1038/s41598-020-70298-2.

[96] L.T.H. Nguyen, J.-S. Hwang, M.-S. Kim, J.-H. Kim, S.-K. Kim, J.-M. Lee, Charpy impact properties of hydrogen-exposed 316l stainless steel at ambient and cryogenic temperatures, Metals (Basel) 9 (6) (May 2019) 625, https://doi.org/10.3390/met9060625.

[97] Y.-H. Nam, J.-S. Park, U.-B. Baek, J.-Y. Suh, S.-H. Nahm, Low-temperature tensile and impact properties of hydrogen-charged high-manganese steel, Int. J. Hydrog. Energy 44 (13) (Mar. 2019) 7000–7013, https://doi.org/10.1016/j.ijhydene.2019.01.065.

[98] K.N. Yoon, H. Oh, J.I. Lee, E.S. Park, Development of low-temperature impact-damage tolerant high entropy alloy with sequential multi-deformation mechanisms, J. Appl. Phys. 133 (17) (May 2023), https://doi.org/10.1063/5.0147689/2887759.

[99] D. Li, Y. Zhang, The ultrahigh charpy impact toughness of forged AlxCoCrFeNi high entropy alloys at room and cryogenic temperatures, Intermetallics (Barking) 70 (Mar. 2016) 24–28, https://doi.org/10.1016/j.intermet.2015.11.002.